MDPI

Article

Wind SRG-Based Bipolar DC Microgrid with Grid-Connected and Plug-In Energy Supporting Functions

Shangping Lin, Yujie Huang and Changming Liaw *

Department of Electrical Engineering, National Tsing Hua University, Hsinchu 300044, Taiwan
* Correspondence: cmliaw@ee.nthu.edu.tw

Abstract: Although a switched reluctance generator (SRG) is not the mainstream wind generator, it possesses the application potential and is worth developing for its many structural merits and high developed power ability. This paper presents a wind SRG-based bipolar DC microgrid having grid-connected and plug-in energy supporting functions. First, a surface-mounted permanent magnet synchronous motor (SPMSM)-driven wind turbine emulator (WTE) is established. Next, the wind SRG with an asymmetric bridge converter is developed. Good generating characteristics are obtained through proper designs of power circuit, commutation mechanism, external excitation source, voltage and current controllers. Third, a DC/DC boost interface converter and a bipolar voltage balancer are constructed to establish the 500 V microgrid bipolar DC-bus. To preserve the microgrid power supplying quality, a battery energy storage system (BESS) with bidirectional DC/DC interface converter is equipped. A dump load leg is added across the bus to limit the DC-bus voltage under energy surplus condition. In load side, a three-phase bidirectional load inverter is developed, which can be operated as a single-phase three-wire (1P3W) inverter or a three-phase three-wire (3P3W) inverter. Good sinusoidal voltage waveform and regulation characteristics are obtained using the proportional-resonant (PR) control. The microgrid to load and microgrid to grid operations are conductible. Finally, to further improve the powering reliability of microgrid, a three-phase T-type Vienna switch-mode rectifier (SMR) based plug-in energy supporting scheme is developed. When the microgrid energy shortage occurs, the possible harvested energy can be used to supply the microgrid.

Keywords: wind generator; SRG; bipolar DC microgrid; BESS; grid-connected; plug-in energy support

1. Introduction

A microgrid [1,2] using renewable energy sources and energy storage devices is helpful for reducing the fossil fuel consumption and carbon-dioxide emission. A DC microgrid can adopt unipolar or bipolar DC-bus [3,4]. Compared to the former, bipolar DC microgrid can provide more voltage levels, larger line power transfer capability, line fault-tolerant capability, and a simpler load converter schematic. For establishing a high-performance bipolar microgrid, some affairs must be treated: (i) choosing suitable interface converters with proper control for the employed renewable source; (ii) using equipment of proper energy storage devices; (iii) all constituted power stages must be properly controlled and coordinated [5,6]; and (iv) voltage balancing control.

As is well known, a wind generator is one of the most commonly employed renewable sources. Basically, a wind generator can be constructed using any kind of electric machines. Compared to the popularly used induction generator and permanent magnet synchronous generator, SRG possesses many merits, such as a rigid structure, without conductors and permanent magnets on rotor, a simple converter, high developed power and having fault-tolerant capability. Hence, this paper is motivated to develop a wind SRG-based DC microgrid and perform its performance enhancement control.

The power generation capability of a SRG is significantly affected by the nonlinear power developing characteristics and back electromotive force (EMF), which is negative to increase the winding current during the demagnetizing period. Some existing research [7,8] concerning the performance improvement of SRG include: (i) commutation control; (ii) excitation control; and (iii) voltage control. The establishment and control of wind SRG can be referred to [9,10]. Among these, a suited commutation angle shift is considered as the most critical issue. With proper commutation, the enhanced current tracking performance, improved energy conversion efficiency, reduced torque ripple and generated voltage ripple can be possessed.

Since the input sources to microgrid are normally fluctuated, the equipment of energy storage devices is required [11]. The most commonly used energy storage devices in medium- and low-scale power systems include a battery [12], super-capacitor [13], flywheel [14], etc. In this paper, the LiFePO4 battery bank (96 V) constructed by two 48 V battery bank in series is employed.

To establish the DC microgrid, DC/DC converters [15–17] play a crucial role to interface various DC sources, energy storage devices and loads. For a two-level DC/DC converter, the voltage balancer [18,19] is needed to establish the bipolar DC-bus.

The PWM inverter [20,21] is an essential interface converter in DC microgrid to yield the AC source for powering loads under microgrid-to-home (M2H) mode or implementing the microgrid-to-grid (M2G)/grid-to-microgrid (G2M) operations. In the established microgrid, the developed 1P3W inverter is used to power the test loads. For obtaining the good AC voltage waveform and dynamic response characteristics under linear/nonlinear and unbalanced loads, the PR control [22,23] is applied. As to M2G/G2M [24,25] operations, the inter-connected operation between microgrid and utility grid can be achieved successfully with the same inverter.

In addition, a T-type Vienna SMR-based plug-in energy support scheme is developed. The possible harvested sources to provide extra energy support for the developed microgrid include three-phase AC, single-phase AC and DC sources. To obtain well-regulated output voltage and good AC line drawn power quality of the SMR, the one-cycle control (OCC) [26] is used. Moreover, the voltage balancing control [27] is also made due to the inherent three-level bipolar voltage structure.

This paper develops a wind SRG-based bipolar DC microgrid battery energy storage, grid-connected and with plug-in energy supporting functions. Except for this section, this paper is organized as follows. Section 2 describes the system configuration of the developed microgrid. The establishment of a SPMSM-driven turbine emulator is presented in Section 3. Then in Section 4, the proposed bipolar DC microgrid is established. The constituted power stages a wind SMR, a boost DC-DC converter followed by voltage balancer leg and a BESS. Section 5 presents the M2H, G2M and M2G operations of the microgrid. In Section 6, the T-type Vienna SMR-based plug-in energy support scheme is introduced. Finally, Section 7 concludes this paper.

2. System Configuration

The system configuration of the established wind SRG-based DC microgrid system is presented in Figure 1. The detailed schematic of the microgrid is depicted in Figure 2a. An inverter-fed SPMSM shown in Figure 2b is employed as a wind turbine emulator.

The experimental wind SRG with a followed asymmetric bridge converter is first established. A two-level boost converter followed by a voltage balancer is developed to establish the bipolar DC-bus. Then, the battery energy storage system and the three-leg 1P3W/3P3W inverter are established with proper controls. The battery storage system can store excessive energy and support the microgrid via the bidirectional one-leg converter. The microgrid can power the home appliance through the 1P3W inverter. On the other hand, it can also be operated as a 3P3W inverter to conduct the bidirectional power transfers between the microgrid and the utility grid.
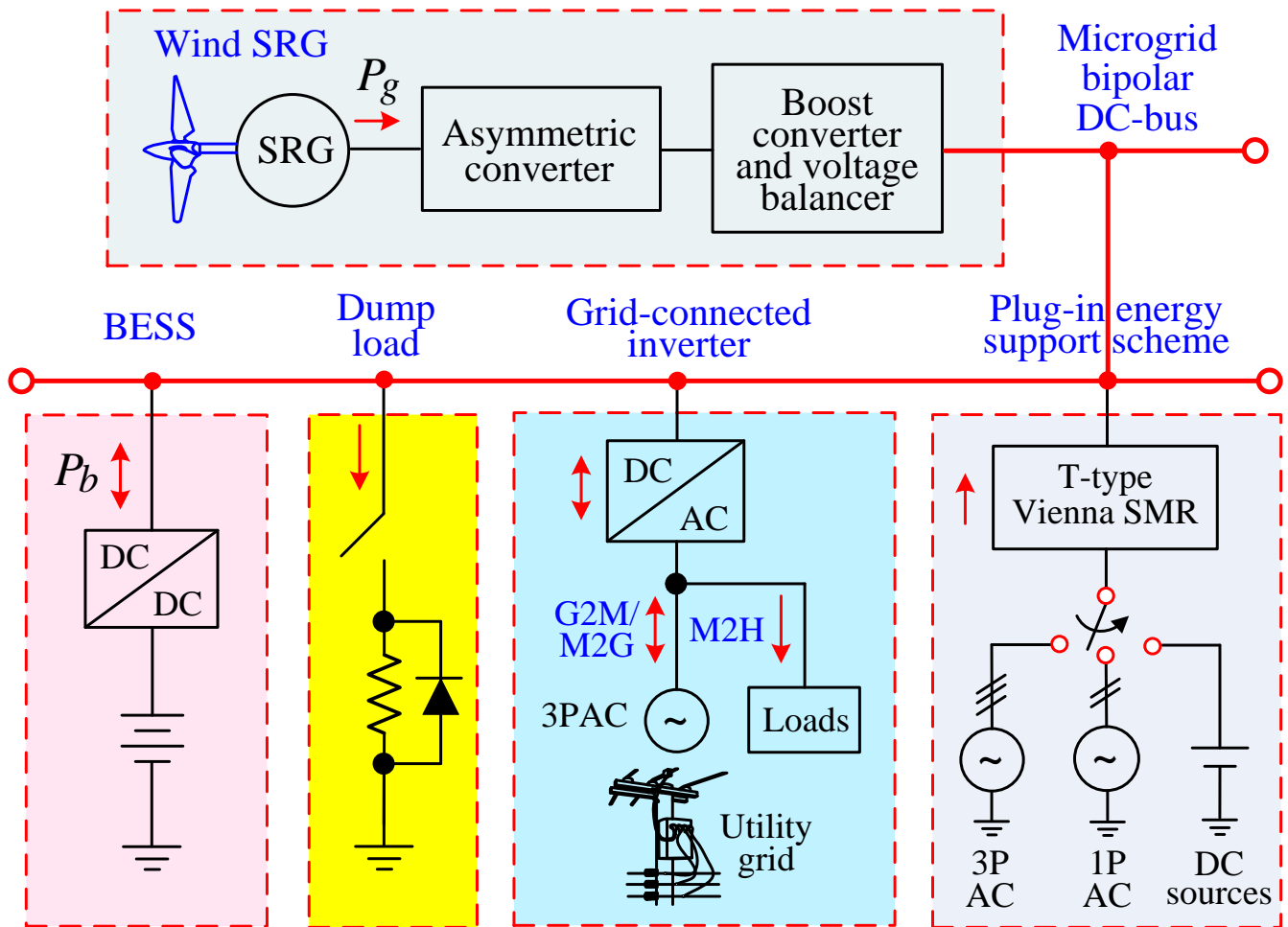
Figure 1. Functional block of the developed wind SRG-based DC bipolar microgrid with grid-connected and plug-in energy support functions.

Finally, a plug-in auxiliary energy support scheme is established. The three-phase three-level T-type Vienna SMR with one-cycle control (OCC) scheme is developed to obtain the well-regulated DC-link voltage and the improved current tracking characteristics. The possible harvested sources include three-phase AC, and single-phase AC and DC sources, and the DC sources may be photovoltaic, fuel cell, and EV battery, etc.

Due to the limit of scope, the detailed designs of all constituted power circuits and control schemes can be referred to [28]. Only a brief description is given in this article.
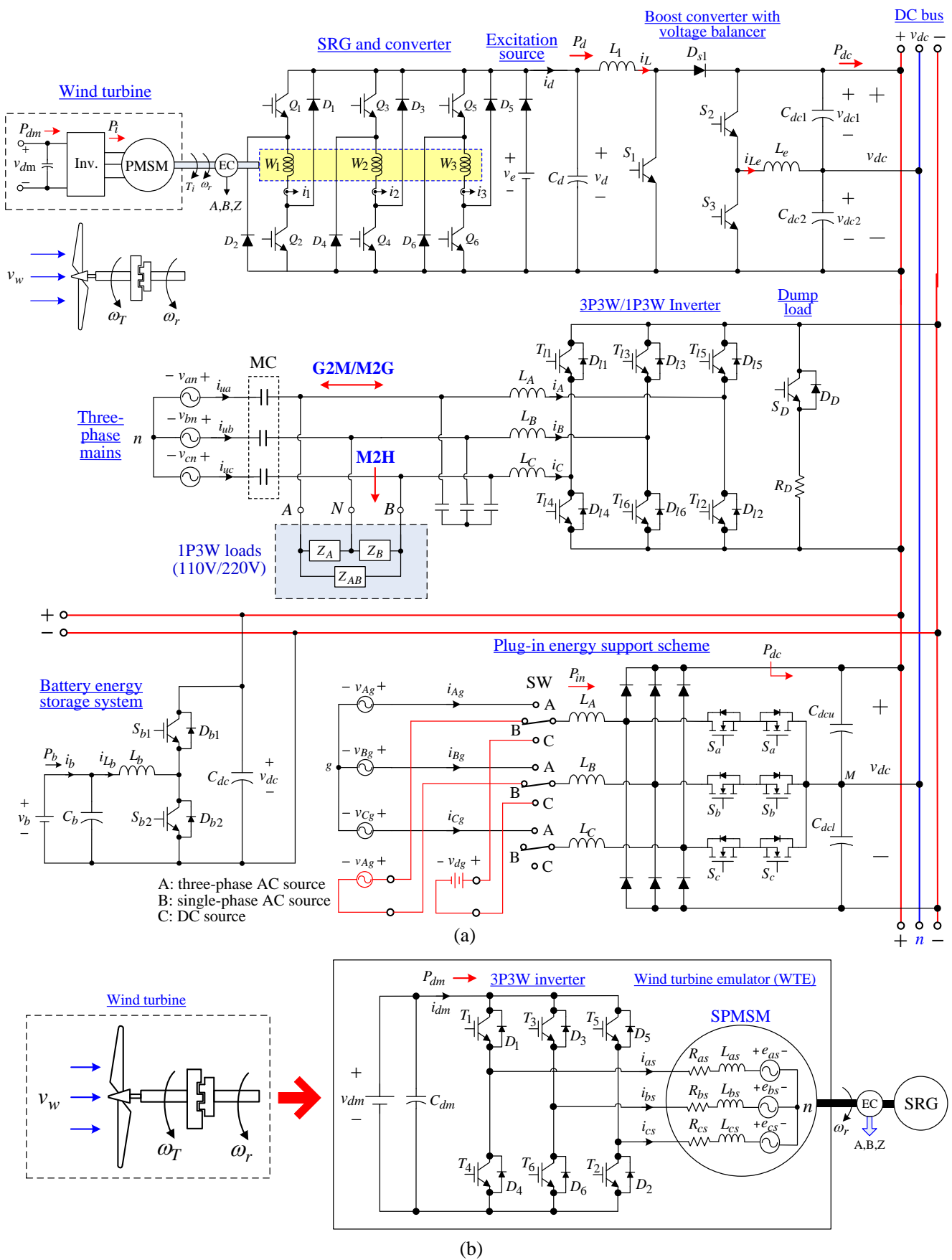
Figure 2. Power circuits of the developed bipolar DC microgrid: (a) microgrid; (b) WTE.

3. PMSM Based Turbine Emulator

For facilitating the development research of a generator system, a faithful turbine emulator is needed. In the developed microgrid, a PMSM-based turbine emulator as shown in Figure 2b is established, which can be operated as a traditional fixed-speed turbine or a variable speed wind turbine. Figure 3 shows the arranged control scheme.
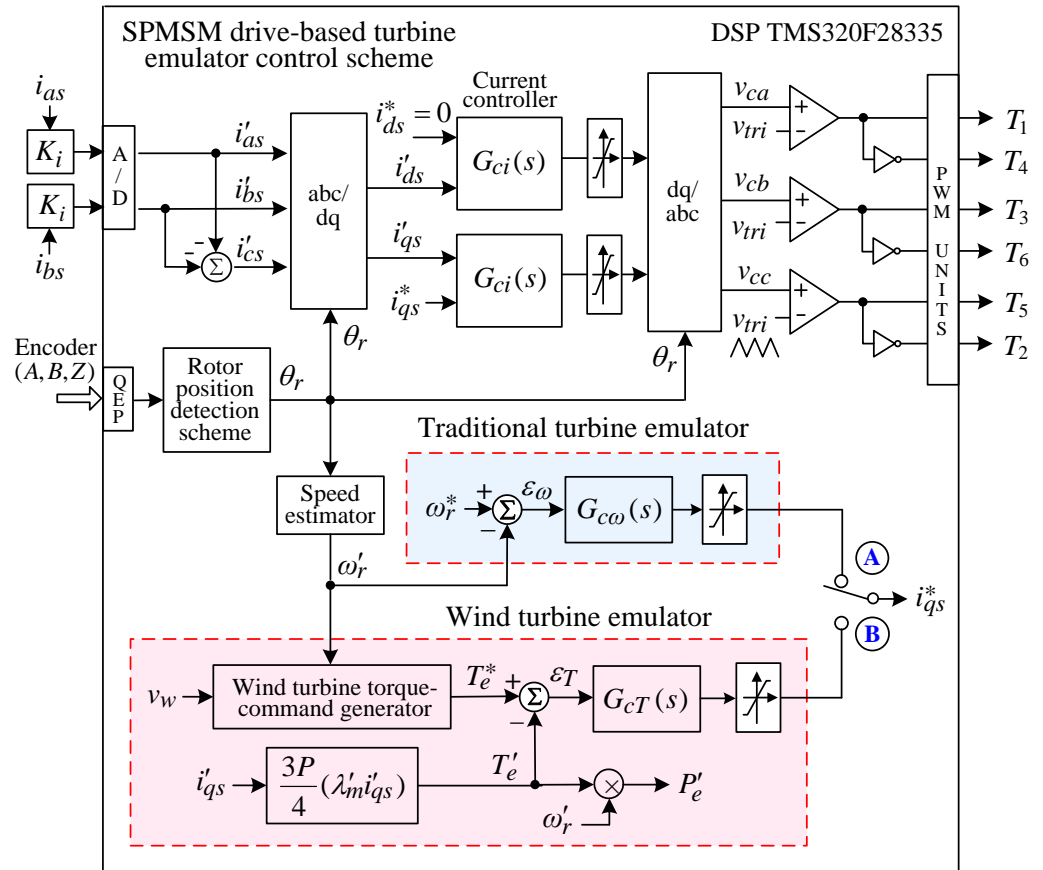
Figure 3. Control scheme of the developed SPMSM-driven turbine emulator.

3.1. Power Circuit

The specifications and major parameters of the employed SPMSM are: (1) 8-pole, 2 kW, 9.6 A, 2000 rpm, 9.8 N-m; (2) armature phase winding resistance $R_s = 0.3\Omega$, arma- ture phase winding inductance $L_s = 2.265mH$, permanent magnet flux linkage $\lambda'_m = 0.1342Wb$. The SPMSM drive three-leg six-switch inverter is constructed using the IGBT module CM100DY-12H ($V_{CES} = 600V$, $Ic_{,avg} = 100A$ $I_{C,peakci} = 200A$) by Mitsubishi Company, Tokyo, Japan.

3.2. Control Scheme

The designed controllers in Figure 3 are listed as follows:

(1) Current feedback controller: $G_{ci}(s) = 2 + 183.32/s$. In the design stage, the P-gain is first determined using the large-signal stability criterion for the ramp-comparison current-controlled PWM (RC-CCPWM) scheme. Then, the I-gain is set via a trial-and-error approach.

(2) Speed feedback controller: $G_{c\omega}(s) = 1.4 + 0.476/s$. The speed loop dynamic model parameters are first estimated using the step-response method. The desired closed-loop tracking transfer function is defined to be $H_{dr}(s) = 1/(1 + 0.1s)$. Then, the controller $G_{c\omega}(s)$ can be derived.

(3) Torque feedback controller: $G_{cT}(s) = 0.4 + 80/s$ which is chosen trail-error-error.
(4) The observed electromagnetic developed torque is: $T'_e = 3P\lambda'_m i'_{qs}$.

3.3. Turbine Emulator
System Configuration

The developed turbine emulator can be operated as a conventional turbine emulator under speed control mode or a WTE under torque mode.

A. Conventional turbine emulator
    The mode switch in Figure 3 is placed at the position "A". The SPMSM drive is operated in speed mode. The torque current command i^*_{qs} is yielded from the outer speed loop. Fixed-speed or varied-speed turbine can also be emulated depending on the specific generator types.

B. Wind turbine emulator
    By placing the switch at the position "B", the motor drive is operated under torque control. The torque command T^*_e is yielded by the wind turbine torque command generator, which generates the torque–speed curve based on a specific wind turbine to be emulated.

Generally, the wind turbine torque-speed characteristics can be represented by a quadratic equation of rotor speed:

$$T_e = a\omega_r^2 + b\omega_r = a\left(\omega_r + \frac{b}{2a}\right)^2 - \frac{b^2}{4a} \tag{1}$$

The power can be expressed as:

$$P_e = a\omega_r^3 + b\omega_r^2 \tag{2}$$

From (1), the rotor speed at the maximum torque $\omega_{mt} = -b/2a$ can be derived. The maximum power occurs at the rotor speed $\omega_{opt} = -2b/3a$ can be found from (2).

The maximum torque occurred at $\omega_r = \omega_{mt}$ is represented as:

$$T_{\max} = K_{\max}\omega_{mt}^2 \tag{3}$$

where $K_{\max}$ is the maximum torque constant.

From (1) and (3), one can find the coefficients a and b as:

$$a = -K_{\max}, \ b = 2K_{\max}\omega_{mt} \tag{4}$$

For meeting the specifications of the employed SPMSM, the $K_{\max}$ is determined using the rated speed (2000 rpm) and torque (9.8N · m) as:

$$K_{\max} = 9.8/2000^2 = 2.45 \times 10^{-6} \text{N} \cdot \text{m}/(\text{r}/\text{min})^2 \tag{5}$$

According to the rated speed of the employed SPMSM and the typical wind speed range, the relationship between v_w and ω_{mt} is set as:

$$v_w = \frac{\omega_{mt}}{100} - 2, \ \omega_{mt} \geq 500 \text{ rpm} \tag{6}$$

To measure the torque–speed and power–speed curves, the emulator is first driven in the speed control mode (SW → "A") as shown Figure 3 at a specific speed under no-load condition. Then the wind turbine emulator is changed to the torque control mode (SW → "B"). The load is gradually changed by increasing the output voltage of SRG until the emulator cannot be afforded anymore. The measured torque–speed and power–speed curves are shown in Figures 4 and 5. The measured results are close to the designed results (not shown here).
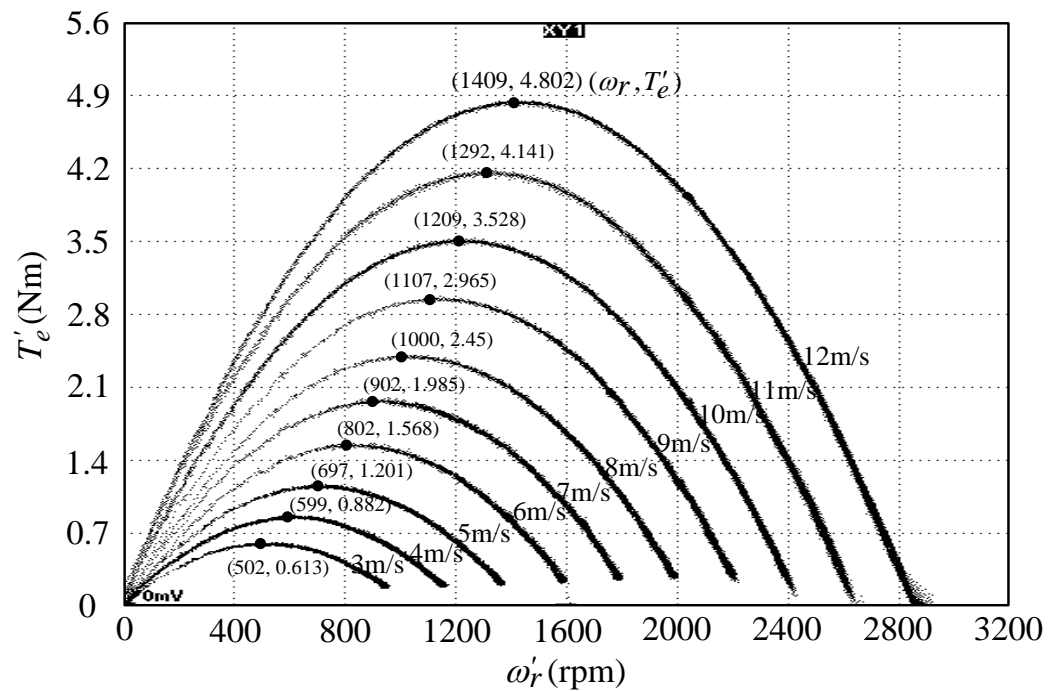
Figure 4. Measured torque–speed curves of the developed wind turbine emulator under various wind speeds.
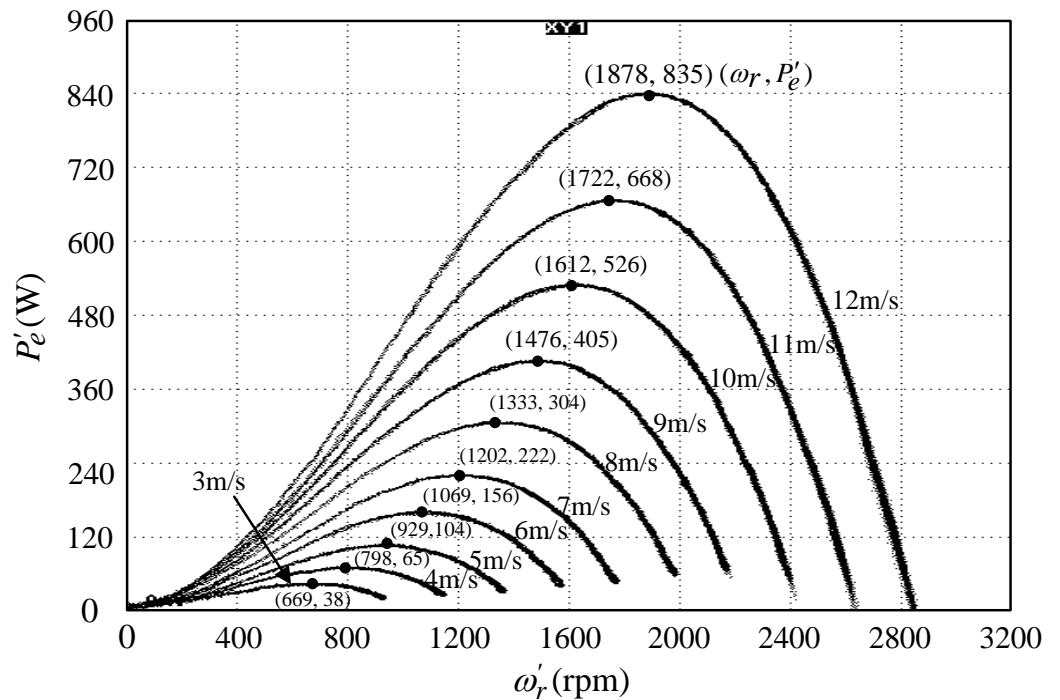
Figure 5. Measured power–speed curves of the developed wind turbine emulator under various wind speeds.

4. Wind SRG-Based Bipolar DC Microgrid

The established wind SRG with asymmetric bridge converter and external excitation source is shown in Figure 2. Through the boost converter with the voltage balancer, the bipolar DC-bus is established, and a dump load leg is equipped to avoid the DC-link over-voltage.

4.1. Wind SRG

4.1.1. Power Circuit

The power circuit components of the developed SRG-based DC microgrid are summarized as follows:

(1) SRG: 3-phase, 12/8, 220 V, 2000 rpm, 1.5 kW;
(2) Asymmetric bridge converter: it is formed using six IGBT modules CM100DY-12H (Mitsubishi) (600 V, 200 A);
(3) Excitation source: the single-phase autotransformer with diode rectifier is used to provide excitation voltage of $v_e = 10V$
(4) Boost converter with voltage balancer: it is consisted of one inductor and three IGBT modules CM100DY-12H;
(5) Dump load: it is constructed by a one-leg IGBT module CM100DY-12H with a dumping resistor of 50 Ω/300 W.

4.1.2. Control Scheme

The control scheme of the established SRG system shown in Figure 6 comprises the outer voltage loop and the inner current loop with the hysteresis current PWM controller (HCCPWM) and commutation shift control scheme. The sampling frequencies of the current loop and the voltage loop are set as 20 kHz and 2 kHz.
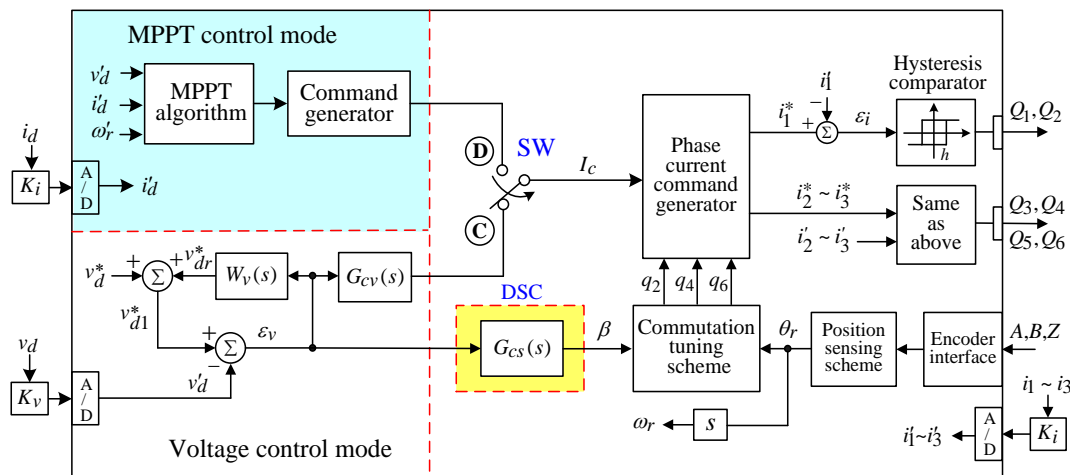
Figure 6. Control scheme of the developed SRG.

The two operation modes are arranged as follows: (i) as the switch is placed at the position "C", the SRG is operated under constant voltage mode for conventional generator; (ii) by placing the switch at "D", the MPPT mode is conducted for a wind generator.

(1) Hysteresis current control scheme
    The hysteresis current-control PWM (HCCPWM) scheme is robust against the system disturbances to reduce the effects of back-EMF of SRG. The hysteresis band is set to be $h = 0.01I_c$, where I_c denotes the SRG winding current command magnitude.
(2) Voltage control scheme
    The voltage feedback controller is augmented with a robust voltage error cancellation controller (RVECC) to enhance the control performance automatically. The voltage sensing factor is set as $K_v = 0.002V/V$, and the designed controller parameters are set below:

    (i) Voltage feedback controller
        At a chosen operating point ($\omega_r = 2000$ rpm, $v_d = 400V$, $R_d = 300\Omega$), the voltage loop dynamic model parameters are first estimated by applying the step-response approach. Then, the desired voltage response due to a step load power change of $\Delta P_d = 533.33W$ ($R_d = 300 \rightarrow 150\Omega$) is specified as:

(maximum dip $\Delta v_{dm} = 8$V, restore time $t_{re} = 0.2$ s). The restore time is defined as $v_d(t = t_{re}) = 0.05\Delta v_{dm}$. Through careful derivation, the feedback controller is found as:

$$G_{cv}(s) = K_{Pv} + \frac{K_{Iv}}{s} = 4.756 + \frac{64.085}{s} \tag{7}$$

(ii)   Robust voltage error cancellation controller (RVECC)

By adding the RVECC, the maximum voltage dip Δv_{dm} yielded by PI feedback control can be reduced by a factor of $(1 - W_v)$, where W_v denotes the robust control weighting factor. However, the resulting control effort will be magnified by $1/(1 - W_v)$. Taking compromised consideration between the control performance and the control effort, the robust control weighting function is set as:

$$W_v(s) = \frac{W_v}{(1 + \tau_v s)} = \frac{0.5}{1 + (1/2\pi \times 0.01538)} \tag{8}$$

4.1.3. Commutation Shift Control Scheme

The generation performance of an SRG is significantly affected by the location of the excited current related to the winding inductance profile $L_1(\theta_r)$. Therefore, a proper commutation shift scheme is necessary to improve the generating characteristics. The defined variables and the current commands i_1^* with the synchronous commutation shift and asynchronous commutation shift of SRG are sketched in Figure 7a,b. The dwell angle is initially set as $\theta_d = 15°$ and the proposed two shifting approaches are further defined as:

(1)   Synchronous commutation shift:

- $\beta_{on} = \beta_{off} = \beta$
- Dwell angle: $\theta'_d = \theta_d = 15°$

(2)   Asynchronous commutation shift:

- $\beta_{on} = 0$, $\beta_{off} = \beta$
- Dwell angle: $\theta'_d = \theta_d + \beta = 15° + \beta$

(3)   Dynamic shift controller (DSC)

To improve the voltage regulation characteristics, the dynamic shifting angle β is determined by regulating the voltage tracking error ε_v through a controller $G_{cs}(s)$. The P-type controller $G_{cs}(s)$ is adopted here:

$$G_{cs}(s) = 0.0166/0.024 = 0.69167 \tag{9}$$
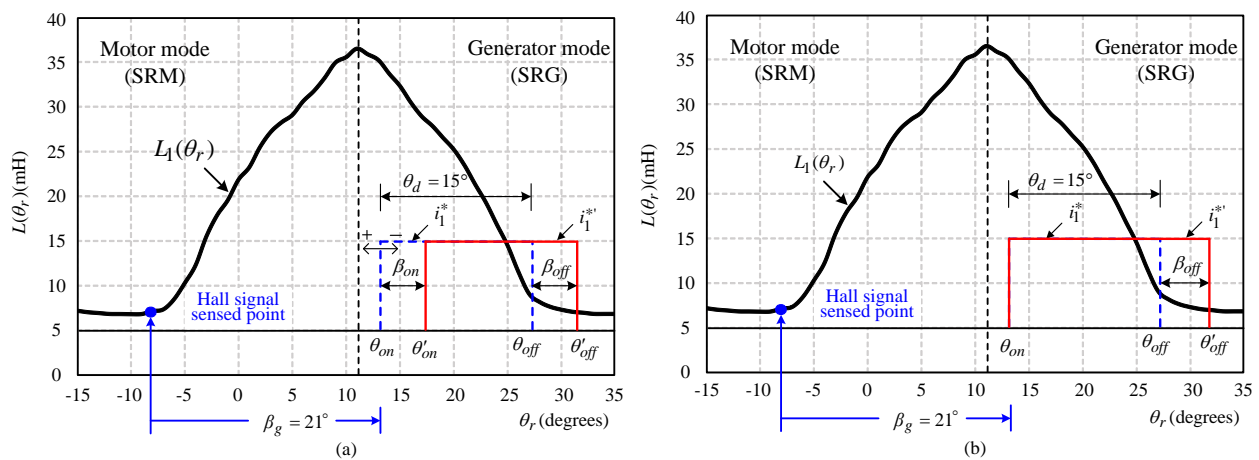
Figure 7. The defined variables and the current commands i_1^* in the commutation process of SRG: (**a**) synchronous commutation shift; (**b**) asynchronous commutation shift.

4.1.4. Measured Results

Figure 8 shows the measured results of the developed SRG by asynchronous shift without and with RVECC at (ω_r =2000rpm, $v_d^* = 400$V) due to a step load resistance change of $R_d = 300 \rightarrow 150\Omega$. The improved regulation response by adding the DSC and further the RVECC can be clearly seen from the results.
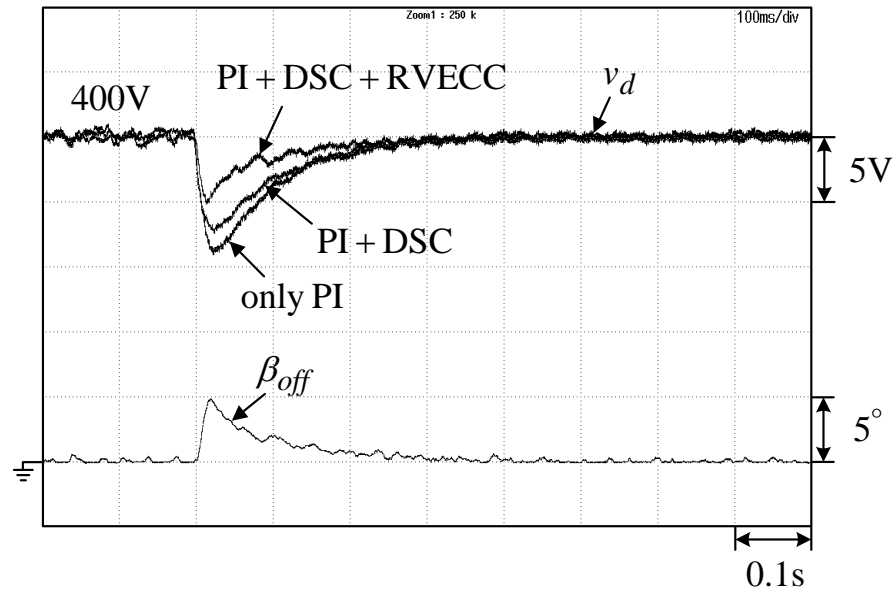
Figure 8. Measured results of the developed SRG by asynchronous shift without and with adding the RVECC at ($v_d^* = 400$V, $\omega_r = 2000$ rpm) due to a step load resistance change of $R_d = 300 \rightarrow 150\,\Omega$.

The generated voltage dynamic characteristics of the developed wind SRG against varying rotor speed are further assessed. Figure 9 shows the measured (ω_r, v_d, i_1) by the asynchronous shift with DSC and RVECC at ($v_d^* = 400$V, $R_d = 300\,\Omega$) under varying speed between ω_r =2000rpm and 1000 rpm. Well-regulated v_d under varying driven speed can be observed.
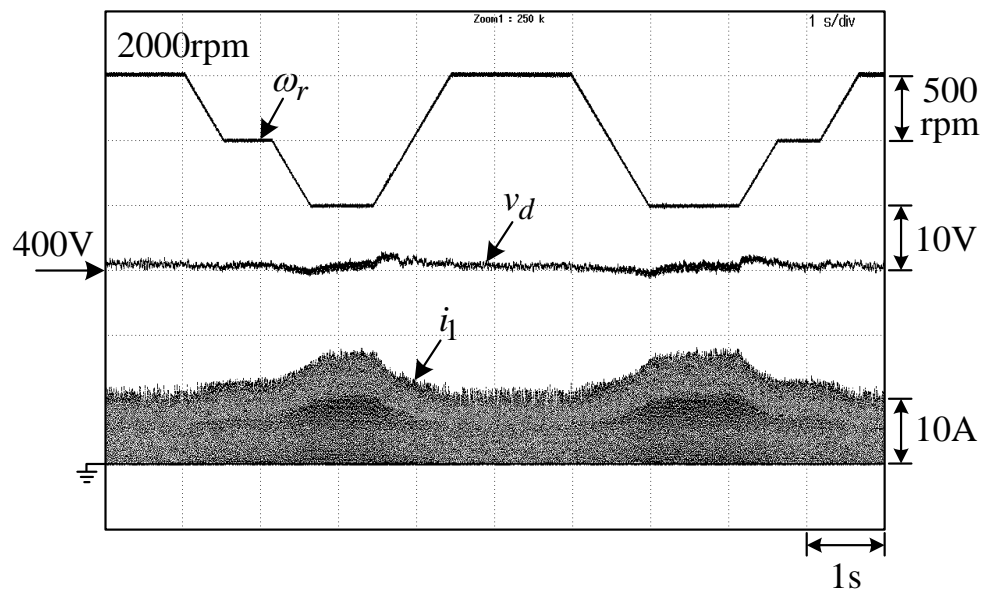
Figure 9. Measured (ω_r, v_d, i_1) of SRG with DSC and RVECC at ($v_d^* = 400$V, $R_d = 300\Omega$) under varying rotor speed $\omega_r = 2000 \rightarrow 1500 \rightarrow 1000 \rightarrow 2000 \rightarrow 1000 \rightarrow 1500 \rightarrow 2000$rpm.

Since the back-EMF of an SRG is directly related to the rotor driven speed, the generated commands are set as: ($v_d^* = 400$V at $\omega_r = 2000$rpm), ($v_d^* = 300$V at $\omega_r = 1500$rpm) and ($v_d^* = 200$V at $\omega_r = 1000$rpm). The measured ω_r and v_d of the SRG with (DSC + RVECC) at $R_d = 300\Omega$ under varying rotor speed are shown in Figure 10.
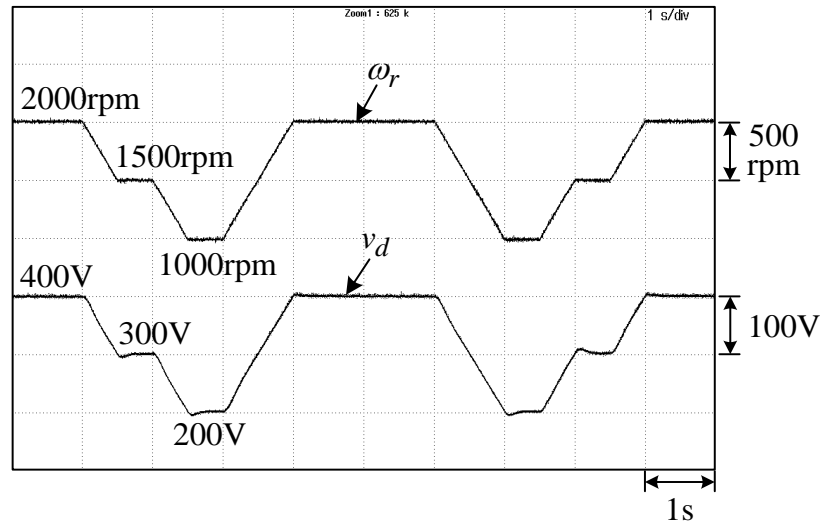
Figure 10. Measured ω_r and v_d of SRG with DSC and RVECC at $R_d = 300\Omega$ under speed-dependent generated voltages with the varying rotor speed $\omega_r = 2000 \rightarrow 1500 \rightarrow 1000 \rightarrow 2000 \rightarrow 1000 \rightarrow 1500 \rightarrow 2000$rpm.

4.1.5. MPPT Control of the Wind Turbine Emulator-Driven SRG

By placing the switch SW in Figure 6 at position "D", the MPPT mode is applied. The winding current command I_c is determined by applying the perturb and observe (P & O) control algorithm to yield the maximum power $P_{d,\max}$. The step size of current command is based on the change of the sensed DC-link power P_d and the SRG rotor speed ω'_r. The directionality judgment of the MPPT control algorithm is shown in Figure 11.

Case 1: $\Delta\omega'_r < 0$ and $\Delta P_d > 0 \Rightarrow \Delta I_c > 0$

Case 2: $\Delta\omega'_r < 0$ and $\Delta P_d < 0 \Rightarrow \Delta I_c < 0$

Case 3: $\Delta\omega'_r > 0$ and $\Delta P_d > 0 \Rightarrow \Delta I_c < 0$

Case 4: $\Delta\omega'_r > 0$ and $\Delta P_d < 0 \Rightarrow \Delta I_c > 0$

Case 5: $\left|\Delta P_d\right| \leq 1$W $\Rightarrow \Delta I_c = 0.025$A
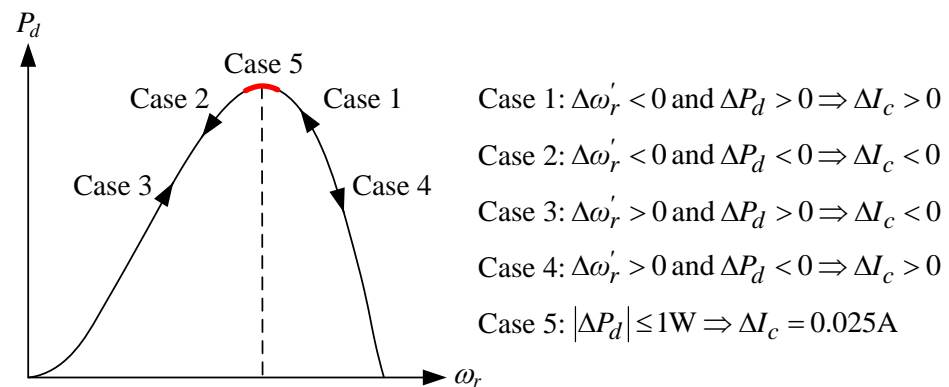
Figure 11. The directionality judgment of the MPPT control algorithm.

To verify the dynamic characteristics of the developed WTE-driven SRG under MPPT control mode, the measured ($\omega'_r, P_e, T'_e, v_d, I_c, P_d, i_1$) when the wind speeds are changed from $v_w = 7$ m/s to $v_w = 8$ m/s and from $v_w = 8$ m/s to $v_w = 7$ m/s are shown in Figure 12. From the measured results, one can observe that the WTE-driven SRG system possesses satisfactory regulation ability and good dynamic tracking characteristics, while changing wind speed can be verified.
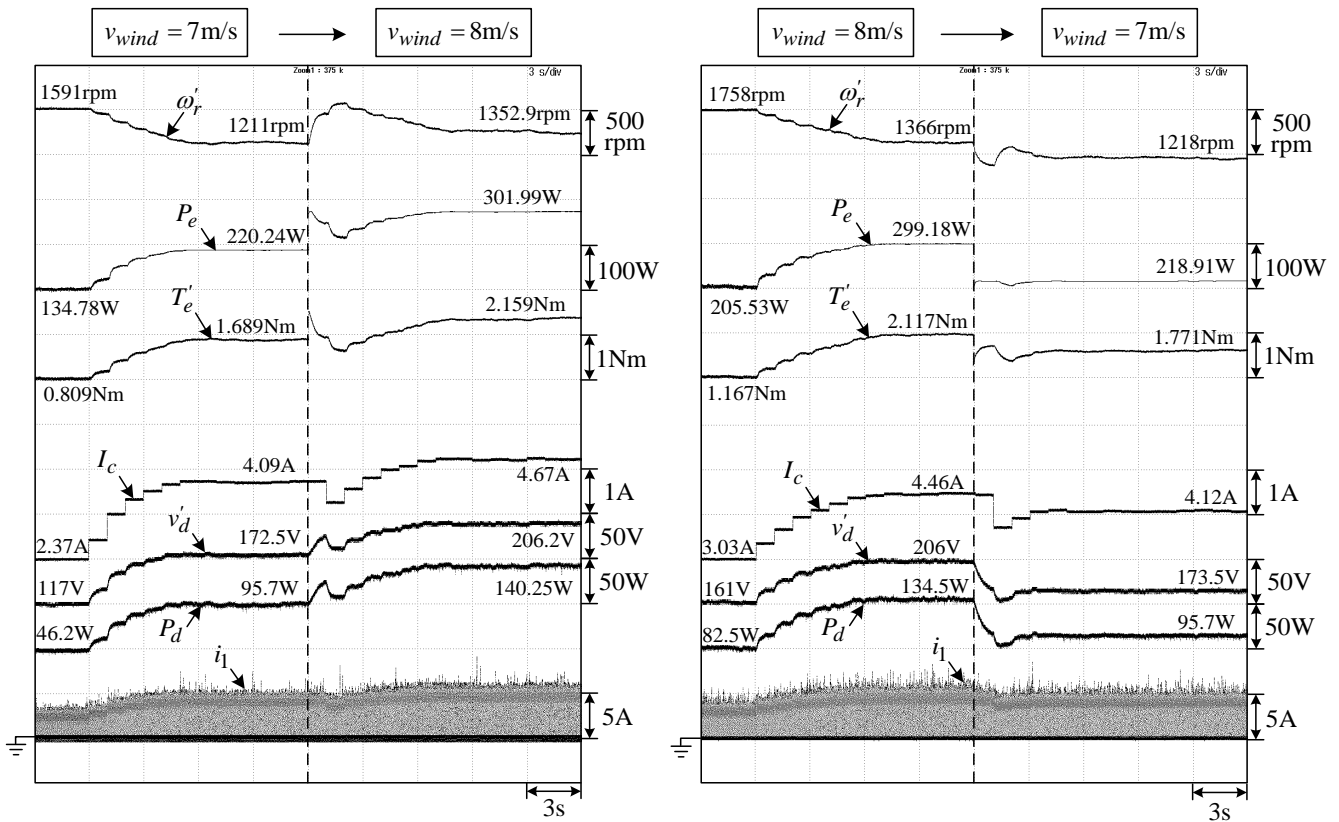
Figure 12. Measured dynamic MPPT algorithm characteristics (ω'_r, P_e, T'_e, v_d, I_c, P_d, i_1) of the developed WTE-driven SRG with an asymmetric bridge converter due to the wind speed change from (v_w =7 m/s to v_w =8 m/s) and (v_w =8 m/s to v_w =7 m/s).

4.2. Two-Level Boost Converter and Three-Level Voltage Balancer

4.2.1. Power Circuit

The boost converter with a voltage balancer shown in Figure 2a consists of two inductors with L_1 = L_e =3.73mH. The calculated current ripple can be found as Δi_L = 1.072A. The output filtering capacitors are chosen to be C_{dc1} = C_{dc2} =2200 μF/400V. Hence, C_{dc} = (2200/2) μF = 1100 μF, and the three IGBT modules CM100DY-12H are used to realize its switches.

4.2.2. Control Scheme

The control scheme of the boost converter and voltage balance shown in Figure 13 comprises outer voltage and inner current loops.
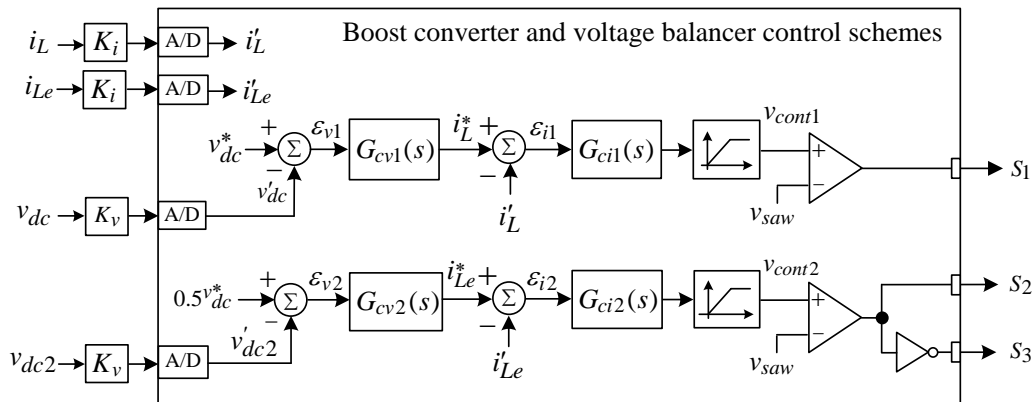
Figure 13. Control schemes of the developed boost converter and voltage balancer.

(1)   Current control scheme

    (i)   Boost converter
           The designed PI current feedback controller is:

$$G_{ci1}(s) = K_{Pi} + \frac{K_{Ii}}{s} = 0.937 + \frac{41.547}{s} \tag{10}$$

           First, the P-gain is determined using the large-signal stability criterion for RC- CCPWM scheme. Then, through the computer-aided simulation for the current loop gain, the controller listed in (10) is found to yield the cross-over frequency f_c and the phase margin (PM) to be (f_c = 2kHz, PM = 89.8°).

    (ii)   Voltage balancer
           Because the current loop possesses an inherent pole at the origin, it is sufficient to adopt the P-type controller as:

$$G_{ci2}(s) = 0.936 \tag{11}$$

           It is found that the cross-over frequency f_c and phase margin (PM) of current loop gain are (f_c = 2kHz, PM = 90°).

(2)   Voltage control scheme

    (i)   Boost converter
           The voltage feedback controller is chosen to be PI type

$$G_{cv1}(s) = 10.75 + \frac{57.52}{s} \tag{12}$$

           The corresponding cross-over frequency and phase margin of voltage loop gain are (f_c = 20Hz, PM = 93.5°).

    (ii)   Voltage balancer
           The voltage controller of the voltage balancer is also chosen as PI type with:

$$G_{cv2}(s) = 33.259 + \frac{125.619}{s} \tag{13}$$

           The resulting cross-over frequency and phase margin of voltage loop gain are (f_c = 20Hz, PM = 89.4°).

4.2.3. Measured Results

    The established whole bipolar DC microgrid system consisting of SRG and followed boost converter stage is operated and evaluated. Figure 14 shows the measured (v_{dc}, v_d, i_L) due to a step load resistance change of $R_{dc} = 500 \rightarrow 250\Omega$. Good regulation responses of the two DC-link voltages can be observed from the results.
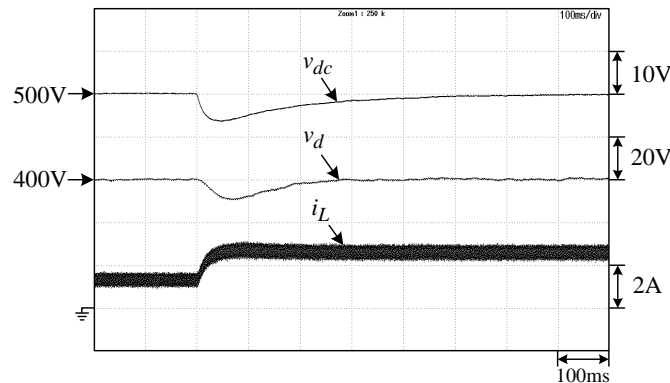
Figure 14. Measured (v_{dc}, v_d, i_L) of developed wind SRG-based DC microgrid due to a step load resistance change of $R_{dc} = 500 \rightarrow 250\Omega$ ($\Delta P_{dc} = 500$W, $V_{dc} = 500$V).

To evaluate the performance of the developed wind SRG-based DC microgrid, two cases are arranged at $(v_{dc} = 500V, R_{dc} = 300\Omega)$: (i) the fixed SRG output voltage $(v_d = 400V)$ is set; (ii) SRG generated voltage is speed-dependent with ratio 0.2 V/rpm from the lowest speed of 1000 rpm $(v_d = 200V)$ to the highest speed of 2000 rpm $(v_d = 400V)$. Figure 15a,b show the measured ω_r, v_d and v_{dc} of the wind SRG-based DC microgrid with fixed and varied v_d under varied rotor speed $\omega_r = 2000 \rightarrow 1500 \rightarrow 1000 \rightarrow 2000 \rightarrow 1000 \rightarrow 1500 \rightarrow 2000$rpm. From the results, well-regulated v_d can be observed.
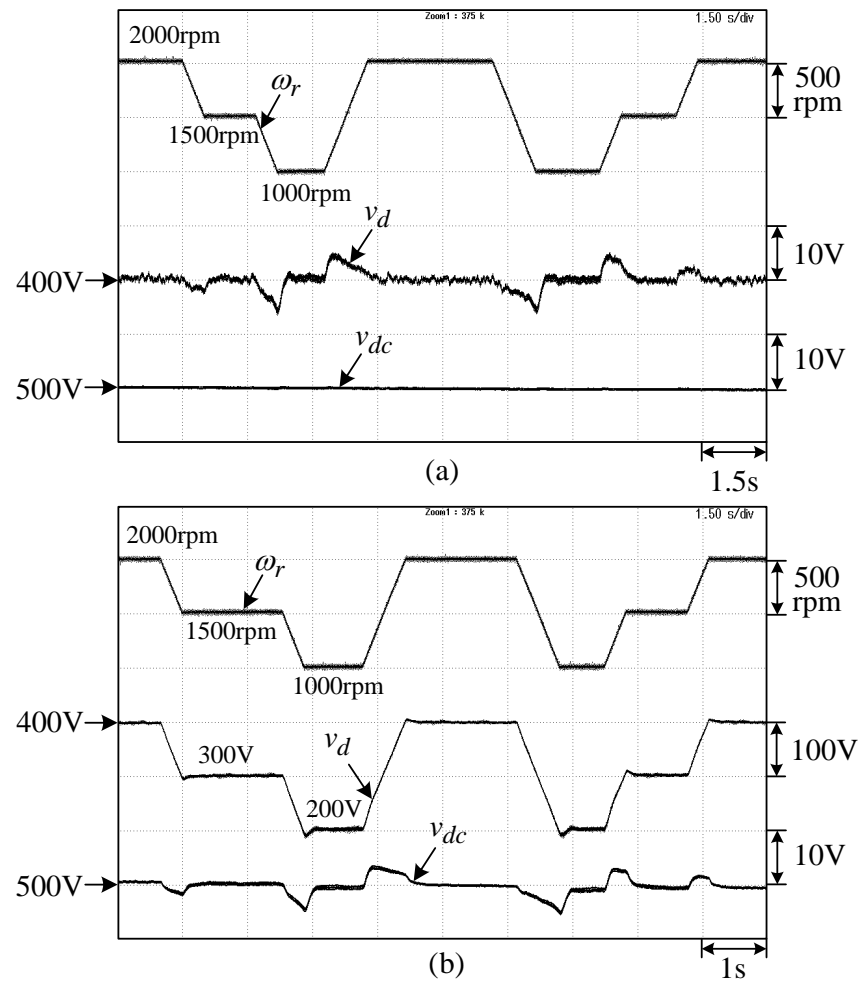
Figure 15. Measured (ω_r, v_d, v_{dc}) of wind SRG-based DC microgrid due to varied speed $\omega_r = 2000 \rightarrow 1500 \rightarrow 1000 \rightarrow 2000 \rightarrow 1000 \rightarrow 1500 \rightarrow 2000$rpm at $(V_{dc} = 500V, R_{dc} = 250\Omega)$: (**a**) fixed $v_d(v_d = 400V)$; (**b**) varied $v_d(0.2 \text{ V/rpm})$.

4.3. Battery Energy Storage System

4.3.1. Power Circuit

The employed LiFePo4 battery pack $(2 \times 48 = 96 \text{ V})$ manufactured by the PHET Company has the following key specifications:

➢ Nominal voltage: 96 V; nominal capacity: 14 Ah;
➢ Maximum charging voltage: 116.8 V; maximum charging current: 14 A;
➢ Maximum discharging current: 28 A; minimum charging voltage: 89.6 V.

The power circuit and control scheme of the developed battery one-leg bidirectional interface converter are shown in Figure 16a,b. The specifications are given as: (i) $f_s = 20$kHz; (ii) $V_{dc} = 500$V; and (iii) $P_{dc} = 1.5$kW.
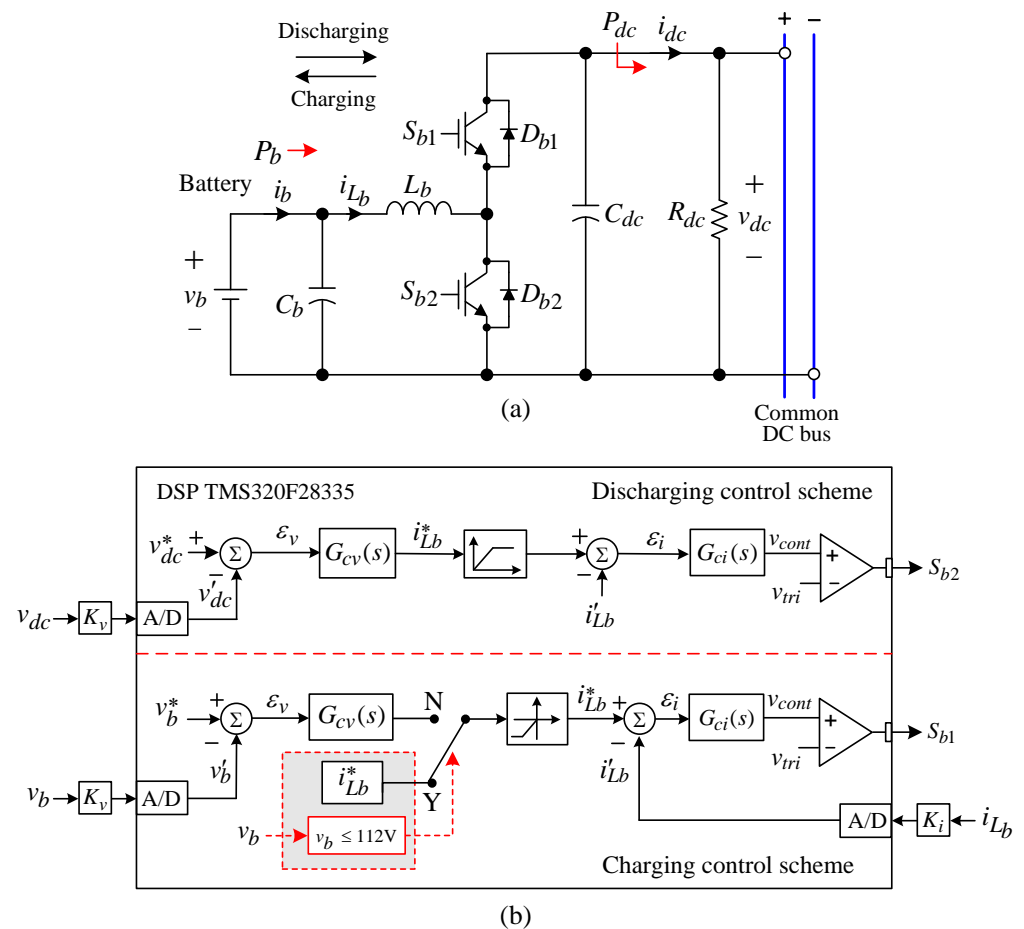
Figure 16. The developed battery one-leg bidirectional DC/DC interface converter: (**a**) power circuit; (**b**) control scheme.

Energy storage inductor: The measured inductance of the used inductor is $L_b = 3.73$mH at 20 kHz. The actual inductor current ripple can be found as: $\Delta i_{L_b} = V_b DT_s / L_b = 96 \times 0.808/(20 \times 3.73) = 1.04$A.

4.3.2. Control Scheme

(1) Current controller

The current controllers in the discharging and charging modes are chosen to be identical, which is designed in discharging mode as:

$$G_{ci}(s) = 1.888 + \frac{177.978}{s} \tag{14}$$

The P-gain is first determined using the large-signal stability criterion for RC-CCPWM scheme. Then, through the computer-aided simulation for the current loop gain, the controller listed in (14) is found to yield the cross-over frequency and the phase margin to be ($f_c = 2$kHz, PM $= 89.6°$).

(2) Voltage controller

The designed controller in discharging mode is:

$$G_{cv}(s) = 21.603 + \frac{78.008}{s} \tag{15}$$

The resulting cross-over frequency and phase margin of voltage loop gain are ($f_c = 20$Hz, PM $= 89.9°$). The controller listed (15) is also employed in the charging mode.

Figure 17 shows the measured (v_b, i_{L_b}) in charging operation under constant current mode (CC mode) and constant voltage mode (CV mode). The battery is charged with constant current ($I_{L_b}^* = 6.5$A), and when the battery voltage reaches 112 V, the constant voltage mode is applied.
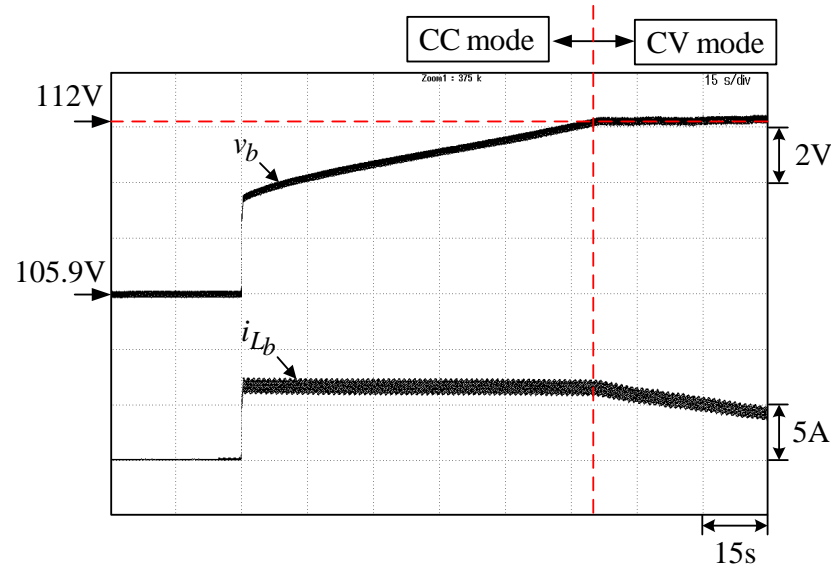
Figure 17. Measured (v_b, i_{L_b}) of the developed battery one-leg bidirectional DC/DC converter in charging buck mode with CC charging and CV charging.

5. Grid-Connected Operations

5.1. Microgrid to Home (M2H) Operation

Single-Phase Three-Wire (1P3W) Inverter

The power circuit and control scheme of the developed 1P3W inverter are shown in Figure 18a,b, which are briefly described as follows.

A.   Power circuit

(1)   DC-bus voltage: $V_{dc} = 500$V;

(2)   AC output voltage: $V_{AN} = V_{NB} = 110$V/60Hz, $V_{AB} = 220$ V/60 Hz;

(3)   1P3W load inverter: three IGBT modules CM100DY-12H are used with output LC filter $L_A = 2.045$mH, $L_B = 2.039$mH, $L_A = 2.043$mH, $C_1 = C_2 = C_3 = 10$μF, which results in the low-pass cut-off frequency of 1113.76 Hz.

B.   Control scheme

The control scheme of the 1P3W in M2H operation is shown in Figure 18b. The DC-link voltage is established by the SRG via an interfaced boost converter with the voltage balancer. The 1P3W inverter consists of a differential mode (DM) leg and a common mode (CM) leg. The former is responsible for controlling the 220 V/60 Hz output voltage v_{AB} and the latter is in charge of balancing the two 110 V/60 Hz output voltages v_{AN} and v_{NB}.

(a)   Current control scheme

The current sensing factor is set as $K_i = 0.05$V/A. To achieve the zero steady-state error for the sinusoidal DM voltage command v_{dm}^*, the proportional-resonant (PR) controller is adopted for all feedback controllers in the proposed control scheme. The controller parameters are set as follows:

(1)   DM controller:

$$G_{cdi}(s) = K_{Pi} + \frac{2K_{Ri}\omega_c s}{s^2 + 2\omega_c s + \omega_r^2} = 1.025 + \frac{(2 \times 40 \times 10)s}{s^2 + 20s + 377^2} \tag{16}$$

The resulted cross-over frequency and phase margin of current loop gain are $(f_c = 2\text{kHz}, \text{PM} = 86.4^\circ)$.

(2)   CM controller:

For CM current control, since L_c is equal to $3L_c$, the common mode current controller can be set by simply increasing the P-gain three times larger than that of the differential mode. Thus:

$$G_{cci}(s) = K_{Pi} + \frac{2K_{Ri}\omega_c s}{s^2 + 2\omega_c s + \omega_r^2} = 3.075 + \frac{(2 \times 40 \times 10)s}{s^2 + 20s + 377^2} \tag{17}$$

(b)   Voltage control scheme

The voltage sensing factor is set as $K_v = 2.5 \times 10^{-3}$ V/V for both DM and CM, and controller parameters are set below:

$$G_{cdv}(s) = G_{ccv}(s) = 1.25 + \frac{(2 \times 40 \times 10)s}{s^2 + 20s + 377^2} \tag{18}$$

The results of the cross-over frequency and phase margin of the voltage loop gain are $(f_c = 1\text{kHz}, \text{PM} = 84.2^\circ)$.
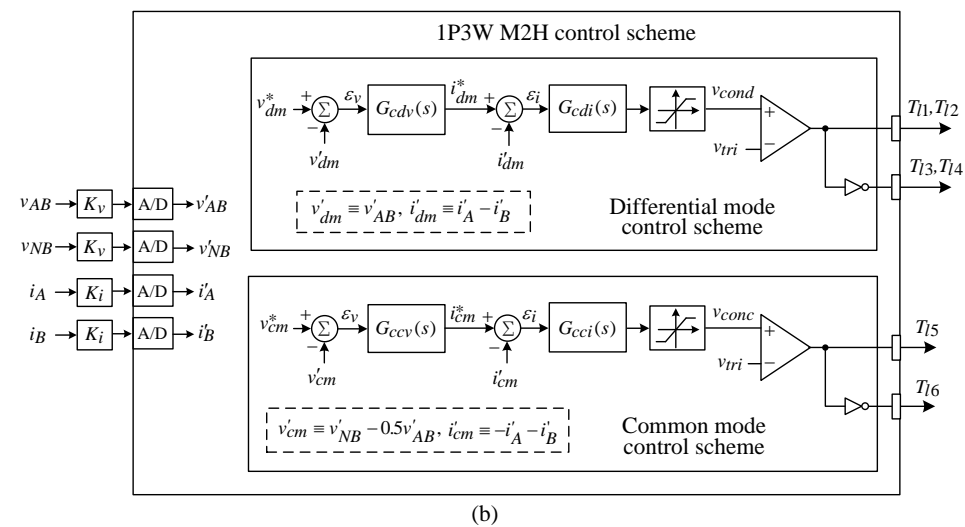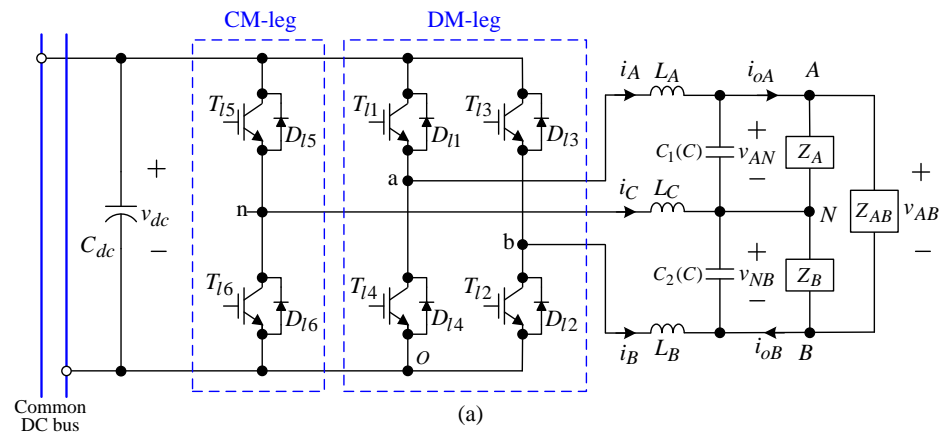
Figure 18. The developed 1P3W inverter in M2H operation: (**a**) power circuit; (**b**) control scheme.

C.   Measured Results

The DM and CM voltage command are set as $v_{dm}^* = 220\text{V}/60\text{Hz}$ and $v_{cm}^* = 0$. The test home appliance loads are depicted in Figure 19. The three cases are:

(1) Case I (unbalanced linear loads): Z_A = incandescent lamp of 115V/60W, Z_B = the incandescent lamps of 120V/100W and 110V/250W, Z_{AB} = the incandescent lamps of 220V/100W;

(2) Case II (nonlinear rectified loads): Z_N = incandescent lamp of 110 V/100 W with C_N = 2200 μF, Z_A = incandescent lamp of 115 V/60 W, Z_B = the incandescent lamps of 120 V/100 W, Z_{AB} = the incandescent lamps of 220 V/100 W;

(3) Case III (reactive loads): Z_A = incandescent lamp of 115 V/60 W, Z_B = the incandescent lamps of 110 V/250 W, Z_{AB} = the incandescent lamps of 220 V/100 W and a single-phase inductor motor at no-load.
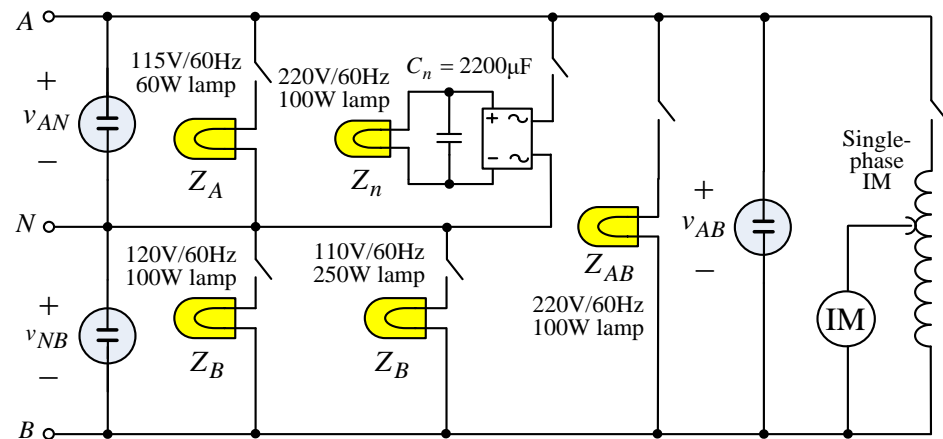
Figure 19. The arranged 1P3W home appliance loads.

Figure 20 shows the measured results of the develop 1P3W inverter under unbalanced linear loads.

5.2. M2G/G2M Operations via 3P3W Inverter

5.2.1. Power Circuit

The schematic of the established inverter for three-phase M2G/G2M operations is depicted in Figure 21. Under G2M operation, the inverter is operated as a three-phase boost SMR to establish the DC-link voltage. As to the M2G operation, the real power and reactive power can be sent to the utility grid via the inverter by directly controlling the q-axis current i_q and d-axis current i_d. The specifications of the developed 3P3W inverter are summarized below:

(a) DC-link voltage: V_{dc} = 500V;
(b) AC output voltage: $V_{ab} = V_{bc} = V_{ca}$ = 220V/60Hz;
(c) PWM switching frequency: f_s = 20kHz;
(d) DC-link capacitors: C_{dc} = 1100μF/1000V (DC);
(e) Output filter: (i) inductors: the measured inductances of the employed inductors under 20 kHz are (L_A = 2.045 mH, L_B = 2.039 mH, L_C = 2.043 mH); (ii) capacitors: $C_1 = C_2 = C$ = 47 pF/400V(AC).

5.2.2. 3P3W Inverter in G2M Operation

A. Control scheme

Figure 22 shows the d-q frame-based control scheme of the 3P3W inverter in G2M operation. The q-axis current i_q is generated by the output of the outer loop voltage controller to regulate the real power component. The d-axis current i_d is set to zero to obtain unity power factor. The control scheme of the 3P3W inverter consists of two inner current loops, one outer voltage loop and a phase-locked loop (PLL).
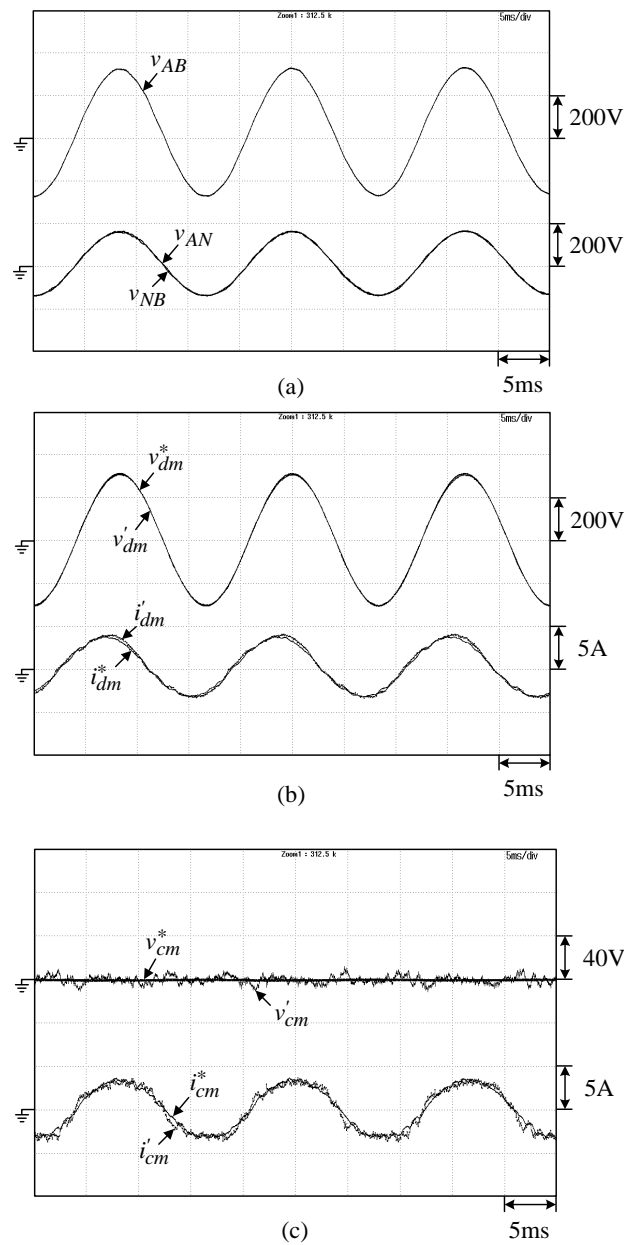
Figure 20. Measured results of the developed 1P3W inverter under unbalanced linear loads: (**a**) (v_{AB}, v_{AN}, v_{NB}); (**b**) v^*_{dm}, v'_{dm},(i^*_{dm}, i'_{dm}); (**c**) (v^*_{cm}, v'_{cm}, i^*_{cm}, i'_{cm}).
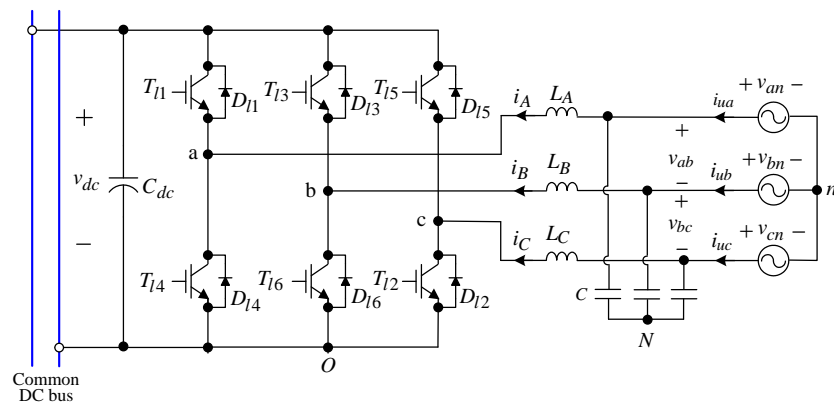
Figure 21. The developed 3P3W inverter in M2G/G2M operations.
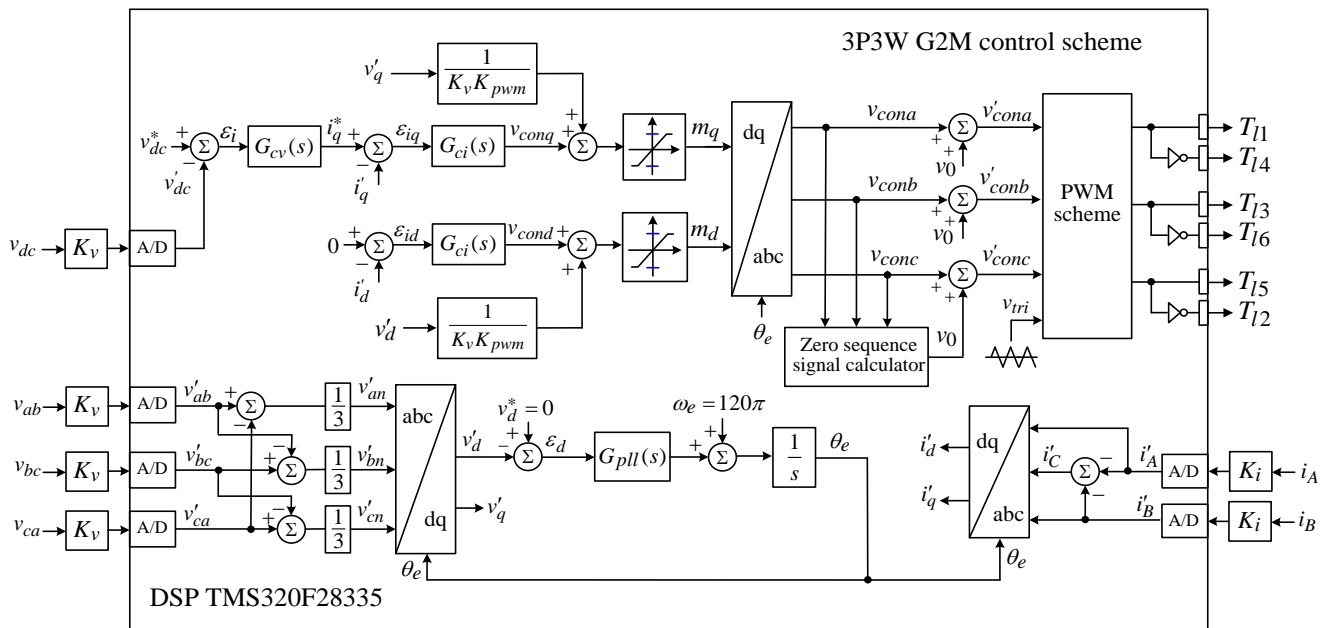
Figure 22. Control scheme of the developed 3P3W SMR in G2M operation.

(a)   PI controller in PLL: it is set as:

$$G_{pll}(s) = K_P + \frac{K_I}{s} = 20 + \frac{250}{s} \tag{19}$$

(b)   Current feedback controller: it is chosen as:

$$G_{ci}(s) = K_{Pi} + \frac{K_{Ii}}{s} = 2.5 + \frac{50}{s} \tag{20}$$

(c)   Voltage feedback controller:

$$G_{cv}(s) = K_{Pv} + \frac{K_{Iv}}{s} = 4.41 + 47.66 \tag{21}$$

At the chosen operating point ($v_{dc} = 500$V, $R_{dc} = 500\Omega$), the PI feedback controller is quantitatively designed to have the desired voltage response with ($\Delta v_{dcm} = 8$V, $t_{re} = 0.25$ s) due to a step load power change of $\Delta P_{dc} = 500$W.

B.   Measured results

To verify the performance of the developed 3P3W inverter in G2M operation, the measured (v_{an}, i_{ua}, i_{ub}, i_{uc}) at ($v_{dc}^* = 500$V, $R_{dc} = 250\Omega$) and labeled power quality parameters are shown in Figure 23. From the results, good AC line drawn power quality can be observed.

5.2.3. 3P3W Inverter in M2G Operation

A   Control scheme

Figure 24 shows the control scheme of the 3P3W inverter in M2G operation. The real power is controlled by the q-axis current i_q, while the reactive power is set by the d-axis current i_d. The current controller and PLL controller parameters are set the same as those in G2M operation.
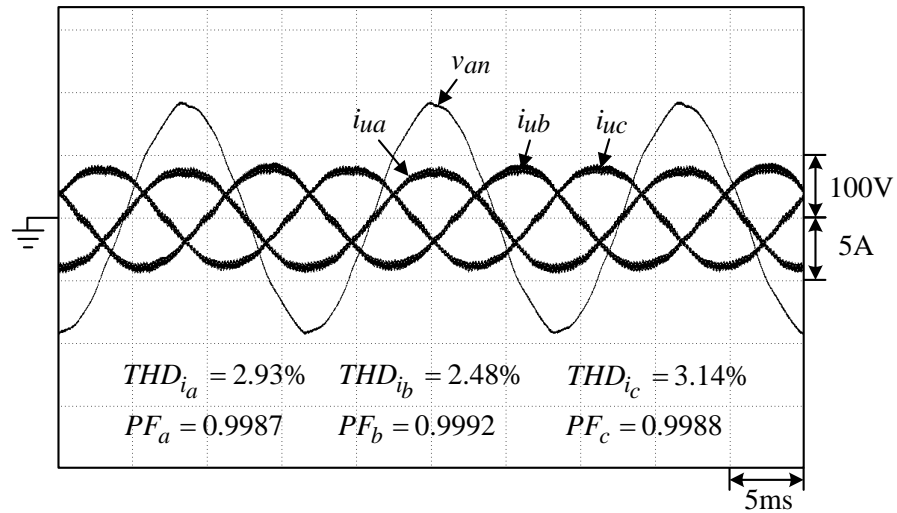
Figure 23. Measured steady-state (v_{an}, i_{ua}, i_{ub}, i_{uc}) of the 3P3W inverter in G2M operation at ($v_{dc}^* = 500V, R_{dc} = 250\Omega$).
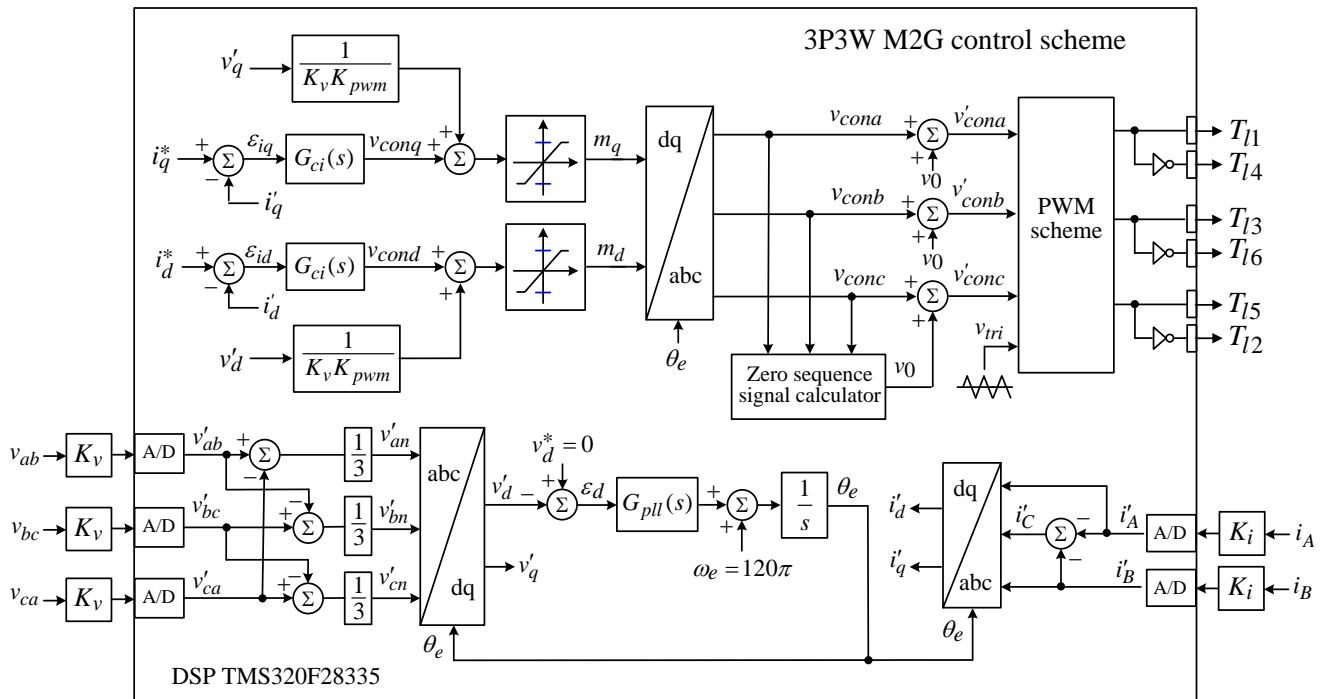
Figure 24. Control scheme of the developed 3P3W inverter in M2G operation.

B.　Measured results

By setting $i_q^* = 4.45$A and $i_d^* = 4.45$A ($P_o = 1.2$kW and $Q_o = 1.2$kVAR), the measured (v_{an}, i_{ua}, i_{ub}, i_{uc}) of the developed 3P3W inverter in M2G operation are shown in Figure 25. From the results, one can be aware that the M2G operation is successfully conducted with the preset real and reactive powers being sent back to the utility grid. The behaviors can be verified from the labeled power factors.

To test the dynamic response of the developed 3P3W inverter, the DC-link $v_{dc} = 500$V is established by a DC power supply. Figure 26 shows the measured dynamic responses of (v_{an}, i_{ua}) due to the step d- and q-axis current command changes. From the measured results, the developed 3P3W inverter possesses good load regulation responses in M2G operation.
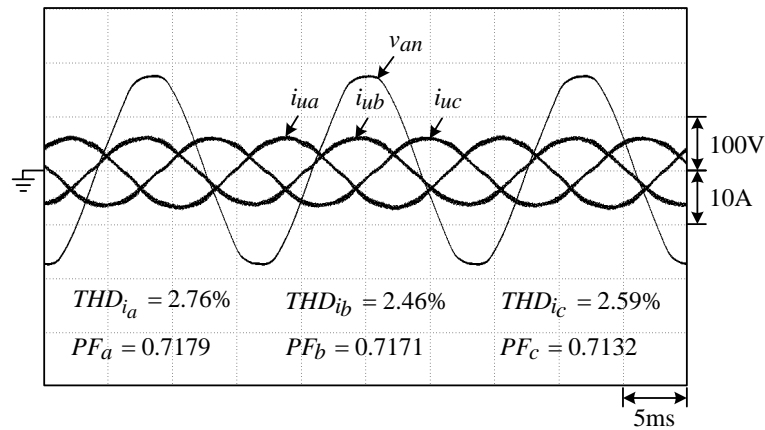
Figure 25. Measured $(v_{an}, i_{ua}, i_{ub}, i_{uc})$ of the 3P3W inverter in M2G operation at $i_q^* = 4.45$A and $i_d^* = 4.45$A ($P_o = 1.2$ kW, $Q_o = 1.2$kVAR).
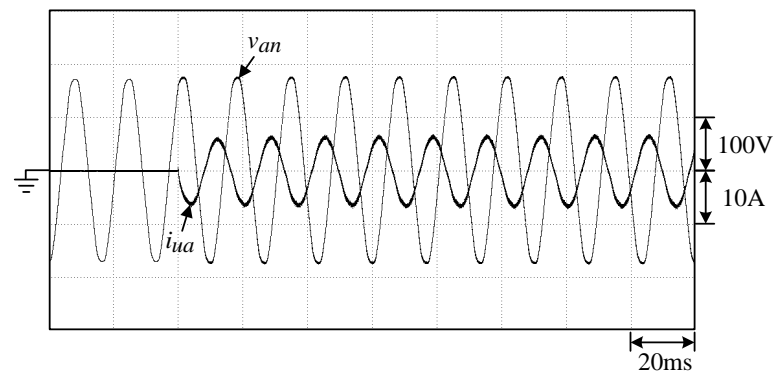
Figure 26. Measured results of the 3P3W inverter under M2G operation due to step current command changes of $i_q^* = i_d^* = 0 \rightarrow 4.45$A ($P_o = 0 \rightarrow 1.2$kW, $Q_o = 0 \rightarrow 1.2$kVAR).

6. Plug-In Energy Support Scheme

The power circuit of the developed T-type Vienna SMR based plug-in energy support scheme is shown in Figures 2a and 27 depicts the control scheme. It mainly consists of the outer voltage loop and the inner OCC-based PWM scheme.
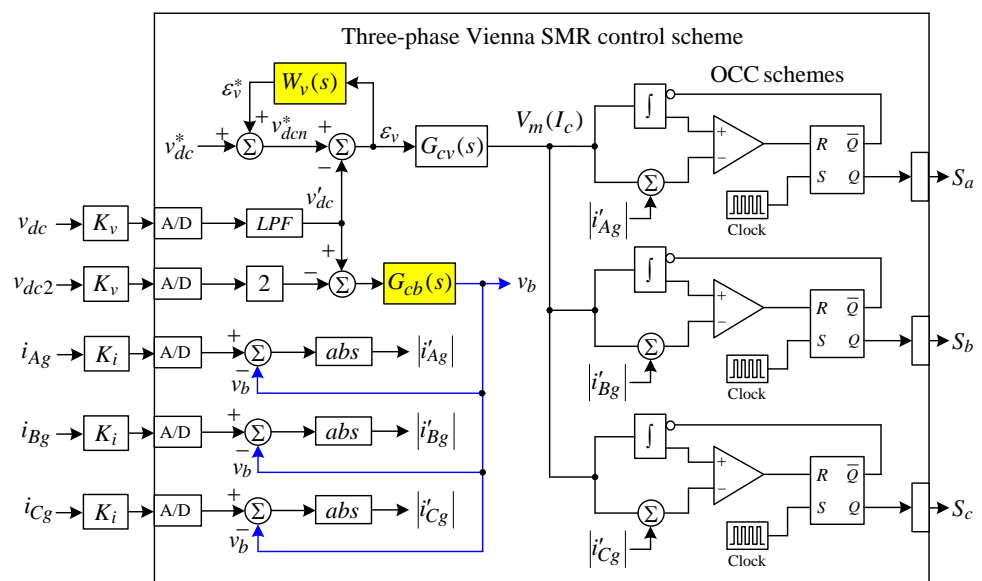
Figure 27. Control scheme of the developed Vienna SMR.

6.1. Three-Phase Vienna SMR

6.1.1. Power Circuit

(1) DC-bus voltage: $V_{dc} = 500V$;

(2) Input AC voltage: three-phase 220V/60Hz;

(3) Boost inductors: $L_A = 1.722mH, L_B = 1.689mH$, $L_C = 1.766mH/20Hz$.

6.1.2. Control Scheme

A. Voltage control scheme

The voltage and current sensing factors are set as $K_v(s) = K_v/(1 + \tau_v s)$, $K_v = 1.667 \times 10^{-3} V/V, \tau_v = 3.98 \times 10^{-4}$. The voltage PI feedback controller in Figure 27 is set as:

$$G_{cv}(s) = K_{Pv} + \frac{K_{Iv}}{s} = 3 + \frac{50}{s} \tag{22}$$

A robust voltage controller is further added to enhance the performance by using a PI controller. The robust control weighting function is set as:

$$W_v(s) = \frac{W_v}{1 + \tau_v s} = \frac{0.5}{1 + 3.98 \times 10^{-4} s}, 0 < W_v < 1 \tag{23}$$

B. Voltage balancing controller

The voltage balancing error ε_v is obtained by subtracting the DC-link voltage from the two times of the lower capacitor voltage. Then, it is regulated by the PI controller $G_{cb}(s)$ to yield the voltage balancing control signal v_b. The controller is set as:

$$G_{cb}(s) = K_{Pb} + \frac{K_{Ib}}{s} = 1 + \frac{30}{s} \tag{24}$$

C. One-cycle control scheme

The OCC scheme for the three-phase Vienna boost SMR is shown in Figure 27. This technique provides a simple solution of PFC without sensing the input voltage. In addition, the multiplier is also not needed. For explanation, the schematic and some sketched waveforms of a one-cycle control scheme are shown in Figure 28a,b.
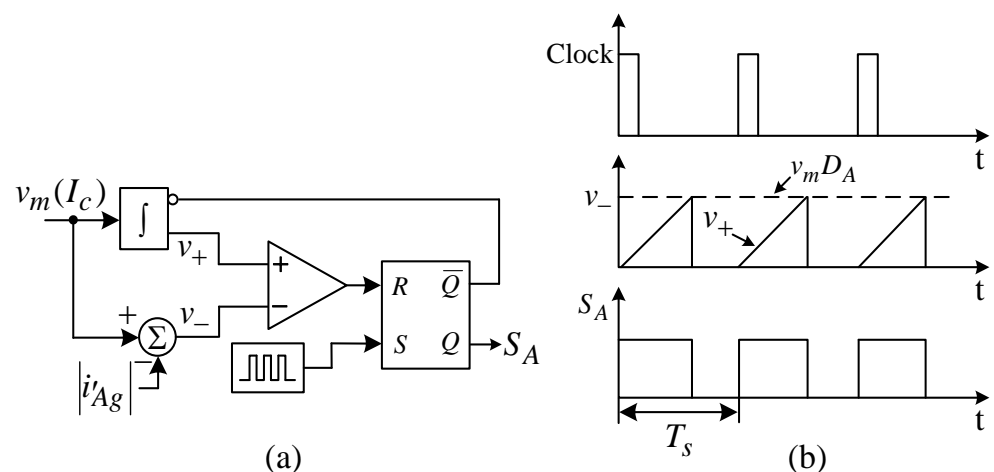
Figure 28. One-cycle control scheme: (**a**) schematic; (**b**) sketched key waveforms.

The single-phase equivalent circuit depicted in Figure 29 is used to illustrate the operation principle of one cycle control for the developed Vienna SMR. To achieve unity power factor, the control goal lies in:

$$|v_{Ag}| = R_{eq}|i_{Ag}| \tag{25}$$

where v_{Ag} = input phase voltage, R_{eq} = single-phase equivalent circuit resistance and i_{Ag} = input phase current.

$$\tilde{V}_{A'g} = \tilde{V}_{Ag} - j\omega_e L_{eq}\tilde{I}_{Ag}$$
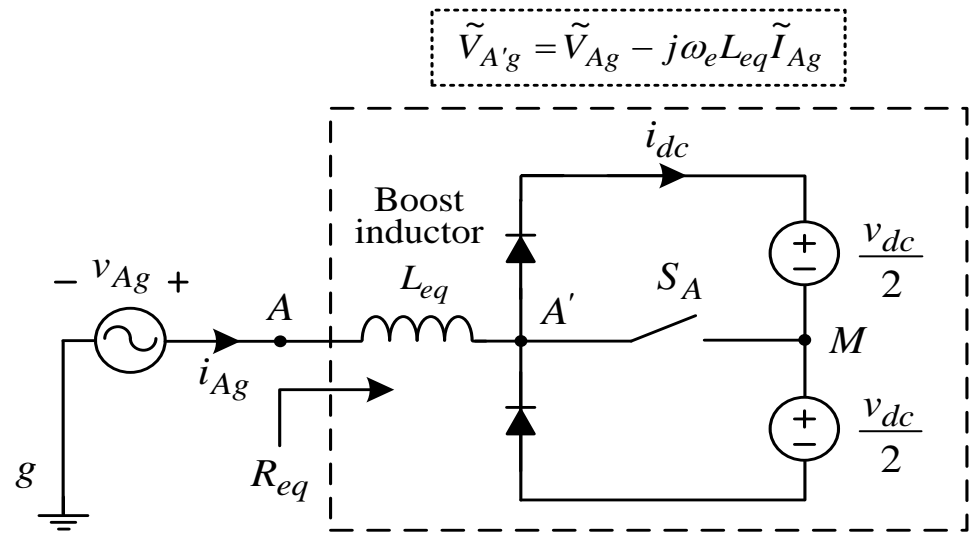
Figure 29. Single-phase equivalent circuit of three-phase Vienna SMR.

The voltage transfer relationship of a Vienna boost SMR is:

$$\frac{v_{dc}}{2}(1 - D_A) = |v_{Ag}| \tag{26}$$

where D_A is the duty ratio of S_A.

From (25) and (26), one can obtain:

$$|i_{Ag}| = \frac{v_{dc}}{2R_{eq}}(1 - D_A) \tag{27}$$

Then, (27) is multiplied with current sensing factor K_i to yield:

$$|i_{Ag}|K_i = |i'_{Ag}|\frac{v_{dc}K_i}{2R_{eq}}(1 - D_A)\Delta\, v_m(1 - D_A) \tag{28}$$

where v_m denotes a modulation voltage generated by the voltage controller. Finally, (28) can be rewritten as:

$$v_m - K_i|i_{Ag}| = v_m D_A \tag{29}$$

According to (29), the key variables set in the developed Vienna SMR to achieve OCC control are $(v_+ = \int v_m dt)$ and $(v_- = v_m D_A)$.

6.1.3. Measured Results

Figure 30 shows the measured $(v_{dc}, i_{Ag}, i_{Bg}, i_{Cg})$ and (v_{Ag}, i_{Ag}) at R_{dc} =120.4 Ω. Figure 31 shows the measured v_{dc} due to a step load change of $(\Delta P_{dc} = 625W)$ with and without robust voltage controller. Significantly improved regulation response can be observed as the robust control is applied. Figure 32 shows the measured (v_{dc1}, v_{dc2}) with and without voltage balancing control under the resistive load $(v_{dc} = 500V, R_{dc} = 120.4Ω)$, the voltage difference between two capacitor (C_{dc1}, C_{dc2}) is quickly eliminated while the voltage balancing control is applied.
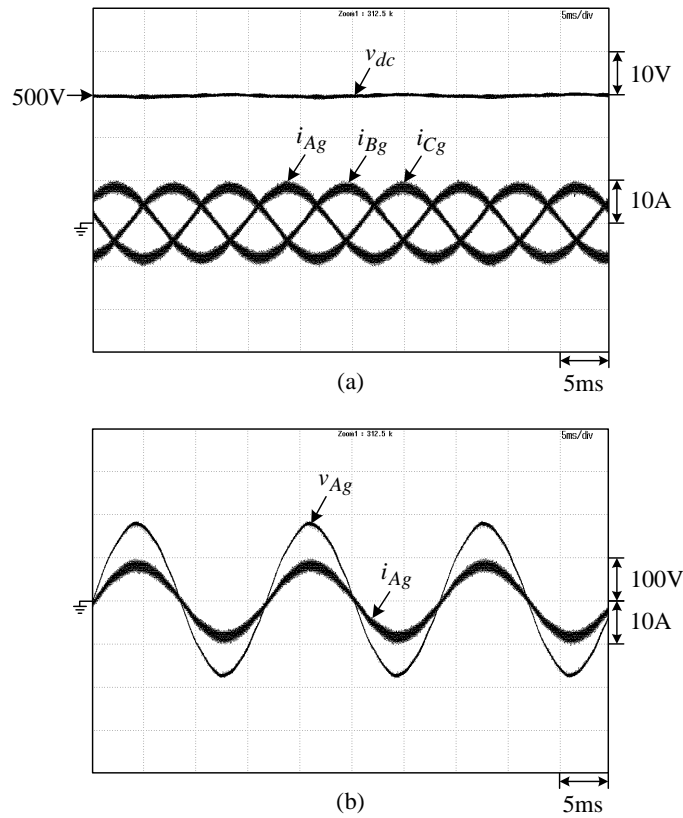
Figure 30. Measured results of the three-phase Vienna SMR under resistive load ($v_{dc} = 500$ V, $R_{dc} = 120.4\Omega$) : (**a**) (v_{dc}, i_{Ag}, i_{Bg},i_{Cg}); (**b**) (v_{Ag}, i_{Ag}).
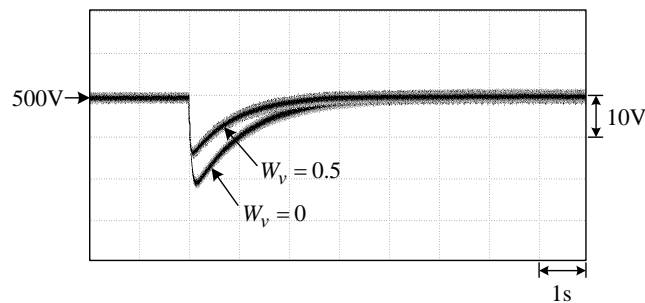
Figure 31. Measured DC output voltage v_{dc} of the developed three-phase Vienna boost SMR due to a load resistance change $R_{dc} = 172.25\Omega \rightarrow 120.4\Omega$ ($\Delta P_{dc} = 625$W) without and with robust control ($W_v = 0, W_v = 0.5$).
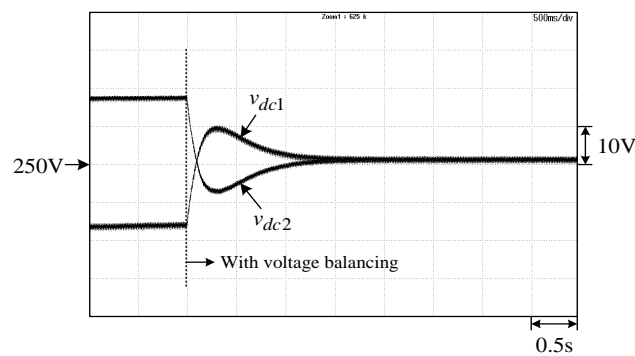
Figure 32. Measured DC output voltages of upper and lower capacitors (V_{dc1}, V_{dc2}) under resistive load ($V_{dc} = 500$V,$R_{dc} = 120.4\Omega$) with and without voltage balancing control.

6.2. Plug-In Energy Support Scheme with Single-Phase AC Input

6.2.1. Power Circuit

The power circuit of the developed Vienna SMR with single-phase AC input shown in Figure 33a is yielded by placing the switches SW in Figure 2a at position "B". Its control scheme is shown in Figure 33b. The system variables and designed power circuit components are summarized as follows:

(1) AC input source: single-phase $v_{ac} =$220 V/60 Hz, $V_m = 311.127$V.
(2) Output rating: $V_{dc} = 500$V, $P_{dc} = 1$kW.;
(3) Output filtering capacitor: $C_{dc} = 1100$μF.;
(4) Switching frequency: $f_{sw} = 20$kHz.;
(5) Energy storage inductor: As shown in Figure 33a, the measured inductances of the two wound inductors are $L_A = 1.722$ mH/20kHz and $L_B = 1.689$mH/20kHz. Hence, the total inductance is $L_A + L_B = 3.411$mH at 20 kHz.

(a)

(b)
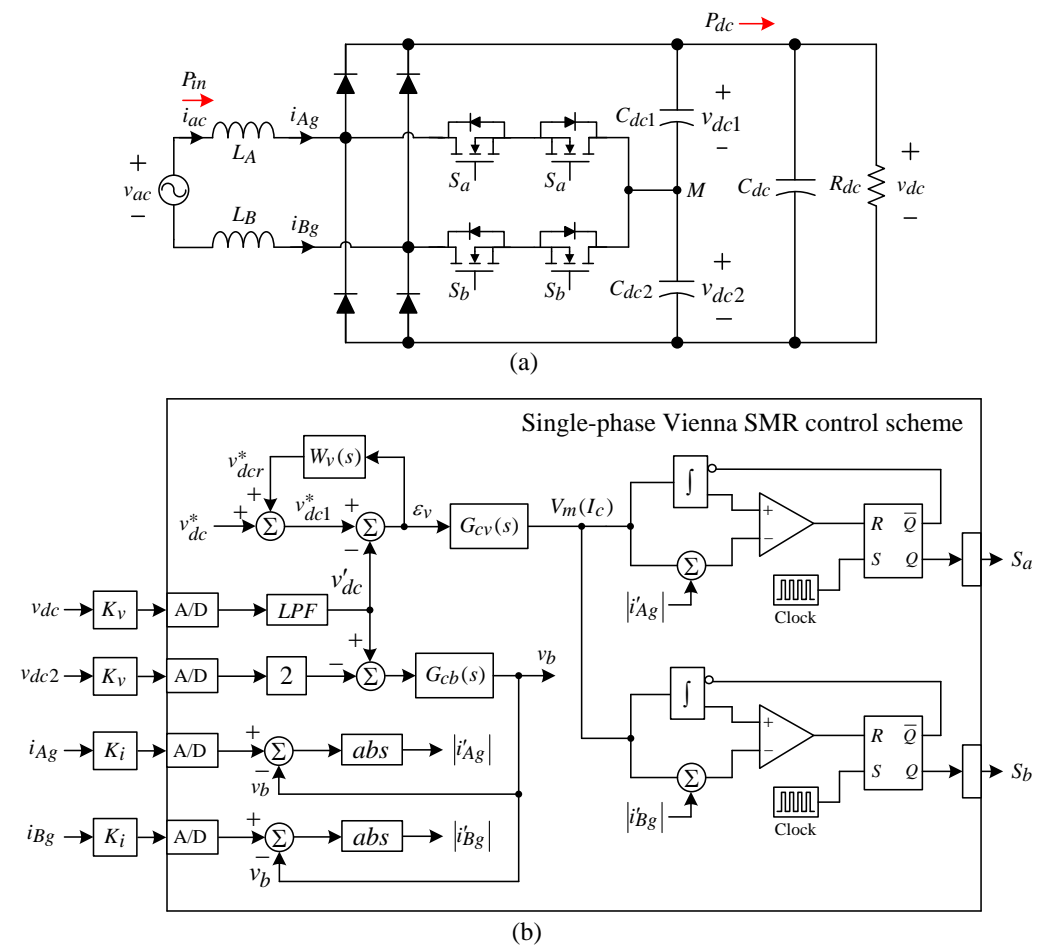
Figure 33. The developed Vienna SMR-based plug-in energy support scheme with single-phase AC source input: (**a**) schematic; (**b**) control scheme.

6.2.2. Control Scheme

In the control scheme Figure 33b, the voltage robust controller and balancing controller are the same as (23) and (24), and the voltage PI feedback controller is set as:

$$G_{cv}(s) = K_{Pv} + \frac{K_{Iv}}{s} = 6 + \frac{120}{s} \tag{30}$$

6.2.3. Measured Results

The measured (v_{dc}, v_{ac}, i_{ac}) of the developed Vienna SMR with single-phase AC input at $(V_{dc} = 500\text{V}, P_{dc} = 1000\text{W})$ are shown in Figure 34. Figure 35 depicts the output voltage due to a step load change of $\Delta P_{dc} = 500\text{W}$ ($R_{dc} = 500\Omega \to 250\Omega$) with and without robust control. Normal operation with satisfactory steady-state and dynamic performances can be seen from the results.
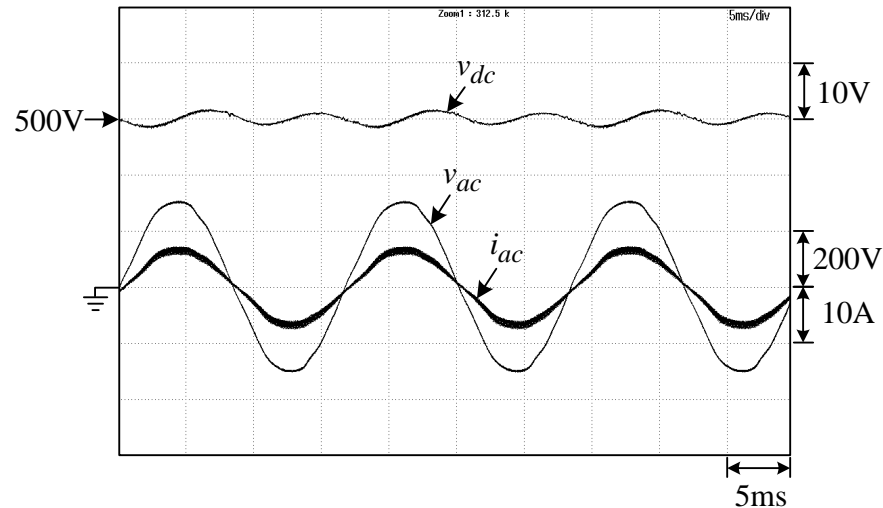
Figure 34. Measured (v_{dc}, v_{ac}, i_{ac}) of the developed Vienna SMR with single-phase AC input at $(V_{dc} = 500\text{V}, P_{dc} = 1000\text{W})$.
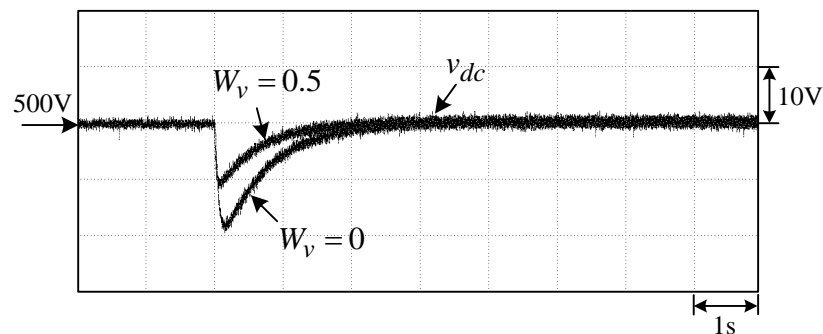
Figure 35. Measured DC output voltage Δv_{dc} of the developed Vienna SMR with single-phase AC input due to a step load change of $\Delta P_{dc} = 500\text{W}$ ($R_{dc} = 500\Omega \to 250\Omega$) without and with robust control ($W_v = 0, W_v = 0.5$).

6.3. Plug-In Energy Support Scheme with DC Input

6.3.1. Power Circuit and Control Scheme

The developed single-phase bridgeless SMR with DC source input and its control scheme are the same as those shown in Figure 33a,b. Only the harvested AC source is replaced by DC source. The robust feedback controller, balancing controller and voltage feedback controller are the same as (22), (23) and (24), respectively.

6.3.2. Measured Results

The measured (v_{dc}, v_{dg}, i_{dg}) of the established Vienna SMR with DC source input at $(V_{dc} = 500\text{V}, V_{dg} = 156\text{V}, R_{dc} = 250\Omega)$ are shown in Figure 36, where $i_{dg} = i_{Ag} = -i_{Bg}$. From the results, the normal operation of the boost DC/DC converter boosting the voltage from 156V to 500V is confirmed.
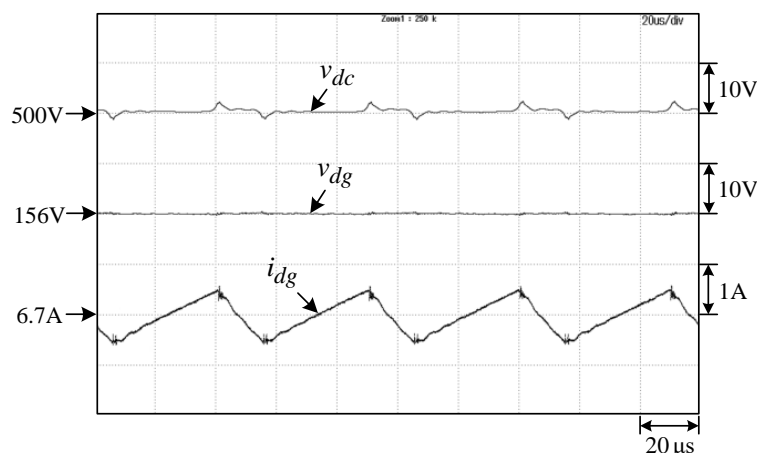
Figure 36. The measured (v_{dc}, v_{dg}, i_{dg}) of the boost DC/DC converter established by the Vienna SMR with DC source input at ($V_{dc} = 500$V, $V_{dg} = 156$V, $R_{dc} = 250\Omega$).

7. Conclusions

This paper has presented the developed wind SRG-based bipolar DC microgrid having grid-connected and plug-in energy supporting capabilities. For driving the studied wind generator, a SPMSM drive-based WTE is first developed. The faithfully emulated wind turbine output behaviors have been verified by measured results. The developed WTE can also be operated as a traditional fixed-speed generator turbine.

Then, the wind SRG followed by the asymmetric bridge converter is established. Through the properly designed power circuit, commutation shifting scheme, current and voltage control schemes, satisfactory wind SRG output characteristics are achieved and demonstrated experimentally. The microgrid bipolar DC-bus is established using a boost DC/DC converter followed by a half-bridge voltage balancer. Well-regulated bipolar DC-bus voltage and good voltage balancing characteristics are obtained by the designed control scheme.

To preserve the microgrid power supplying quality, A BESS with properly designed bidirectional interface converter is equipped. Normal operation of the established BESS has been verified by some measured results. In addition, a dump load leg is added to avoid the bus overvoltage as the energy surplus occurs.

In the load side, a three-leg PWM 1P3W inverter with 220 V/110 V AC voltages is constructed to perform the M2H operation powering the home appliances. The DM/CM control schemes and the PR feedback controller are employed to have good sinusoidal voltage waveforms and load regulation characteristics. The same three-leg inverter can also be operated as a grid-connected 3P3W inverter to conduct the M2G and G2M bidirectional operations.

Moreover, to further improve the reliability of the microgrid and enhance the energy utilization, a plug-in energy support scheme developed to harvest the possible energies, including the three-phase AC source, single-phase AC source and DC source. The T-type Vienna SMR is employed as the infrastructural schematic.

Wind SRG possesses the application potential due to its structural advantages without conductors and permanent magnets on rotor. Moreover, the SRG may have a highly developed power ability while under proper control. The presented key performance enhancement control approaches for SRG are worth mentioning. The suggested further research includes: (i) a practicability research for an actual wind SRG system with practically high ratings; (ii) efficiency enhancement under widely varied wind speed and load ranges; (iii) equipment of the hybrid energy storage system consisting of energy type battery and power type, super-capacitor or flywheel; (iv) multiple sources including photovoltaic and fuel cell; and (v) the incorporated operation of the electric vehicle to microgrid to further enhance the renewable source utilization.

Glossary

Symbol	Unit	Description
A, B, Z		encoder signals
C_b	F	battery side filtering capacitor
C_{dm}	F	SMR output filtering capacitor
C_d	F	generator output filtering capacitor
C_{dc}, C_{dc1}, C_{dc2}	F	converter output filtering capacitors
f_s	Hz	switching frequency
$G_{cb}(s)$		voltage feedback controller
$G_{cci}(s)$		common mode current feedback controller
$G_{ccv}(s)$		common mode voltage feedback controller
$G_{cdi}(s)$		differential mode current feedback controller
$G_{cdv}(s)$		differential mode voltage feedback controller
$G_{ci}(s), G_{ci1}(s), G_{ci2}(s)$		current feedback controllers
$G_{cs}(s)$		dynamic shift controller
$G_{cT}(s)$		torque feedback controller
$G_{cv}(s), G_{cv1}(s), G_{cv2}(s)$		voltage feedback controllers
$G_{c\omega}(s)$		speed feedback controller
$G_{ci}(s)$		closed current loop transfer function
h		hysteresis band
I_c	A	current command magnitude
i_{as}, i_{bs}, i_{cs}	A	winding currents of SPMSM
$i'_{as}, i'_{bs}, i'_{cs}$	A	sensed winding currents of SPMSM
i_d	A	SRG output current
i_{dc}	A	DC-link current
i_{ds}	A	d-axis current
i_{ds}^*	A	d-axis current command of PMSM
i'_{ds}	A	sensed d-axis current of PMSM
i_i	A	phase-i winding current
i'_i	A	sensed phase-i winding current
i_i^*	A	phase-i winding current command
i_L	A	boost converter inductor current
i'_L	A	sensed boost converter inductor current
i_L^*	A	inductor current command
i_{Lb}	A	battery interface converter inductor current
i'_{Lb}	A	sensed battery interface converter inductor current
i_{Lb}^*	A	battery interface converter inductor current command
i_{Le}	A	voltage balancer inductor current
i'_{Le}	A	sensed voltage balancer inductor current
i_{qs}	A	q-axis current
i_{qs}^*	A	q-axis current command
i'_{qs}	A	sensed q-axis current
i_{ua}, i_{ub}, i_{uc}	A	3P3W mains line currents
i_{Ag}, i_{Bg}, i_{Cg}	A	Vienna SMR AC input currents
K_I, K_{Ib}, K_{Ii}		integral gains of controllers

K_{Iv}		integral gain of voltage loop controller
K_i	V/A	current sensing factor
$K_P K_{Pb}, K_{Pv}, K_{Pi}$		proportional gains of controllers
K_{PWM}		PWM scheme transfer ratio
K_{Ri}		resonant controller gain
K_v		voltage sensing factor
$L(i, \theta_r)$	H	SRM winding incremental inductance
L_d	H	d-axis winding inductance
L_{md}	H	d-axis magnetizing inductance
L_{mq}	H	q-axis magnetizing inductance
L_q	H	q-axis winding inductance
L_s	H	armature phase winding inductance
P_b	W	battery output power
P_i	W	inverter output power
P_d	W	asymmetric bridge converter output power
P_{dc}	W	microgrid output power
P_{dm}	W	inverter input power
P_e	W	developed power of wind turbine SPMSM
P_m	W	wind turbine developed power
$Q_1 \sim Q_6$		converter switches of SRG
q_2, q_4, q_6		SRG commutation signals
R_d	Ω	generator side load resistance
R_{dc}	Ω	microgrid side load resistance
R_{dm}	Ω	SMR side load resistance
R_s	Ω	SPMSM winding resistance
S		switch of boost SMR
S_a, S_b, S_c		switches of Vienna SMR
S_{b1}, S_{b2}		switches of one-leg DC/DC converter
S_{e1}, S_{e2}		switches of voltage balancer
T'_e		SPMSM electromagnetic developed torque
T_e^*		torque command
T_e		SRG total developed torque
$T_{l1} \sim T_{l6}$		switches of 1P3W/3P3W inverter
$T_1 \sim T_6$		switches of SPMSM inverter
V_d	V	average SRG output bus voltage
V_{dc}	V	average common DC-bus voltage
V_e	V	SRG excitation voltage
v_{Ag}, v_{Bg}, v_{Cg}	V	Vienna SMR AC input phase voltages
v_{ac}	V	AC input voltage
v_b	V	battery voltage
v_{cont}	V	control signal
v_d	V	SRG output DC-link voltage
v_{dg}	V	DC source input voltage of plug-in energy support scheme
v_{dm}	V	inverter input DC-link voltage
v'_d	V	sensed SRG output DC-link voltage
v_d^*	V	SRG output DC-link voltage command
v_{dc}	V	DC-bus voltage
v'_{dc}	V	sensed DC-link voltage
v_{dc}^*	V	DC-link voltage command
v_{dr}^*	V	compensation voltage command
v_{ds}^*	V	d-axis voltage command
v_{qs}^*	V	q-axis voltage command
v_o	V	zero sequence voltage
v_{saw}	V	saw-tooth carrier
v_{tri}	V	triangular carrier
v_w	m/s	wind speed

W_v		robust control weighting factor
$W_v(s)$		robust control weighting function
Z_A, Z_{AB}, Z_B, Z_n	Ω	1P3W inverter load impedances
α_1, α_2		real poles of system dynamic model
β	rad	SRG commutation shift angle
β_{off}	rad	$\theta'_{off} - \theta_{off}$
β_{on}	rad	$\theta'_{on} - \theta_{on}$
β_p	degree	blade pitch angle
ε_i	V	current tracking error
ε_v	V	voltage tracking error
ε_ω	V	speed tracking error
η	%	efficiency
λ'_m	Wb	PM flux linkage of PMSM
ω_c	rad/s	cut-off angular frequency
ω_{mt}	rpm	shaft speed at maximum torque of wind turbine
ω_{opt}	rpm	optimal shaft speed of wind turbine
ω_r	rpm	SRG shaft speed
τ_v	sec	time constant of low-pass filter for voltage sensing
θ_d	degree	SRG dwell angle
θ_{off}	degree	SRG commutation turn-off angle
θ'_{off}	degree	SRG shifted commutation turn-off angle
θ_{on}	degree	SRG commutation turn-on angle
θ'_{on}	degree	SRG shifted commutation turn-on angle
θ_r	degree	rotor angular position

References

1. Nejabatkhah, F.; Li, Y.W. Overview of power management strategies of hybrid AC/DC microgrid. *IEEE Trans. Power Electron.* **2015**, *30*, 7072–7089. [CrossRef]
2. Dragièeviæ, T.; Lu, X.; Vasquez, J.C.; Guerrero, J.M. DC microgrids—Part II: A review of power architectures, applications, and standardization issues. *IEEE Trans. Power Electron.* **2016**, *31*, 3528–3549.
3. Kakigano, H.; Miura, Y.; Ise, T. Low-voltage bipolar-type DC microgrid for super high quality distribution. *IEEE Trans. Power Electron.* **2010**, *25*, 3066–3075. [CrossRef]
4. Gu, Y.; Li, W.; He, X. Analysis and control of bipolar LVDC grid with DC symmetrical component method. *IEEE Trans. Power Syst.* **2016**, *31*, 685–694. [CrossRef]
5. Dragièeviæ, T.; Lu, X.; Vasquez, J.C.; Guerrero, J.M. DC microgrids—part I: A review of control strategies and stabilization techniques. *IEEE Trans. Power Electron.* **2016**, *31*, 4876–4891.
6. Lema, M.; Pavon, W.; Ortiz; Asiedu-Asante, A.B.; Simani, S. Controller coordination strategy for DC microgrid using distributed predictive control improving voltage stability. *Energies* **2022**, *15*, 5442. [CrossRef]
7. Torrey, D.A. Switched reluctance generators and their control. *IEEE Trans. Ind. Electron.* **2002**, *49*, 3–14. [CrossRef]
8. Chang, Y.C.; Liaw, C.M. On the design of power circuit and control scheme for switched reluctance generator. *IEEE Trans. Power Electron.* **2008**, *23*, 445–454. [CrossRef]
9. Santos Barros, T.A.D.; Santos Neto, P.J.D.; Filho, P.S.N.; Moreira, A.B.; Filho, E.R. An approach for switched reluctance generator in a wind generation system with a wide range of operation. *IEEE Trans. Power Electron.* **2017**, *32*, 8277–8292.speed. [CrossRef]
10. Neto, P.J.D.S.; Barros, T.A.D.S.; Paula, M.V.D.; Souza, R.R.D.; Filho, E.R. Design of computational experiment for performance optimization of a switched reluctance generator in wind system. *IEEE Trans. Energy Convers.* **2018**, *33*, 406–419. [CrossRef]
11. Barton, J.P.; Infield, D.G. Energy storage and its use with intermittent renewable energy. *IEEE Trans. Energy Convers.* **2004**, *19*, 441–448. [CrossRef]
12. Sattar, A.; Al-Durra, A.; Caruana, C.; Debouza, M.; Muyeen, S.M. Testing the performance of battery energy storage in a wind energy conversion system. *IEEE Trans. Ind. Appl.* **2020**, *56*, 3196–3206. [CrossRef]
13. Rocabert, J.; Capó-Misut, R.; Muñoz-Aguilar, R.S.; Candela, J.I.; Rodriguez, P. Control of energy storage system integrating electrochemical batteries and supercapacitors for grid-connected applications. *IEEE Trans. Ind. Appl.* **2019**, *55*, 1853–1862. [CrossRef]
14. Cimuca, G.O.; Saudemont, C.; Robyns, B.; Radulescu, M.M. Control and performance evaluation of a flywheel energy-storage system associated to a variable-speed wind generator. *IEEE Trans. Ind. Electron.* **2006**, *53*, 1074–1085. [CrossRef]
15. Mohan, N.; Undeland, T.M.; Robbins, W.P. *Power Electronics Converters, Applications and Design*, 3rd ed.; John Wiley & Sons, Inc.: Hoboken, NJ, USA, 2003.
16. Tan, N.M.L.; Abe, T.; Akagi, H. Design and performance of a bidirectional isolated DC-DC converter for a battery energy storage system. *IEEE Trans. Power Electron.* **2011**, *27*, 1237–1248. [CrossRef]

17. Hegazy, O.; Mierlo, J.V.; Lataire, P. Analysis, modeling, and implementation of a multi device interleaved DC/DC converter for fuel cell hybrid electric vehicles. *IEEE Trans. Power Electron.* **2012**, *27*, 4445–4458. [CrossRef]
18. Wang, F.; Lei, Z.; Xu, X.; Shu, X. Topology deduction and analysis of voltage balancers for DC microgrid. *IEEE Trans. Emerg. Sel. Top. Power Electron.* **2017**, *5*, 672–680. [CrossRef]
19. Ganjavi, A.; Ghoreishy, H.; Ahmad, A.A. A novel single-input dual-output three-level DC–DC converter. *IEEE Trans. Ind. Electron.* **2018**, *65*, 8101–8111. [CrossRef]
20. Chiang, S.J.; Liaw, C.M. Single-phase three-wire transformerless inverter. *IEE Proc. Electr. Power Appl.* **1994**, *141*, 197–205. [CrossRef]
21. Blasko, V.; Kaura, V. A new mathematical model and control of a three-phase AC-DC voltage source converter. *IEEE Trans. Power Electron.* **1997**, *12*, 116–123. [CrossRef]
22. Teodorescu, R.; Blaabjerg, F.; Liserre, M.; Loh, P.C. Proportional-resonant controllers and filters for grid-connected voltage-source converters. *IEE Proc. Electr. Power Appl.* **2006**, *153*, 750–762. [CrossRef]
23. Chou, M.C.; Liaw, C.M. Dynamic control and diagnostic friction estimation for a PMSM driven satellite reaction wheel. *IEEE Trans. Ind. Electron.* **2011**, *58*, 4693–4707. [CrossRef]
24. Wang, F.; Duarte, J.L.; Hendrix, M.A.M. Grid-interfacing converter systems with enhanced voltage quality for microgrid application—Concept and implementation. *IEEE Trans. Power Electron.* **2011**, *26*, 3501–3513. [CrossRef]
25. Mueller, J.A.; Rasheduzzaman, M.; Kimball, J.W. A model modification process for grid-connected inverters used in islanded microgrids. *IEEE Trans. Energy Convers.* **2016**, *31*, 240–250. [CrossRef]
26. Wang, C.; Liu, J.; Cheng, H.; Zhuang, Y.; Zhao, Z. A modified one-cycle control for Vienna rectifiers with functionality of input power factor regulation and input current distortion mitigation. *Energies* **2019**, *12*, 3375. [CrossRef]
27. Kolar, J.W.; Drofenik, U.; Zach, F.C. Current Handling Capability of the Neutral Point of a Three-Phase/Switch/Level Boost-Type PWM (Vienna) Rectifier. In Proceedings of the 27th Annual IEEE Power Electronics Specialists Conference, Baveno, Italy, 23–27 June 1996; IEEE: New York, NY, USA, 1996; Volume 2, pp. 1329–1336.
28. Lin, S.P. A wind switched-reluctance generator based bipolar DC microgrid with plug-in auxiliary energy support. Master Thesis, Department of Electrical Engineering, National Tsing Hua University, Hsinchu, Taiwan, 2022.